Fast Operator Splitting Methods for Nonlinear PDEs

AN ABSTRACT
SUBMITTED ON THE FIFTEENTH DAY OF APRIL, 2016
TO THE DEPARTMENT OF MATHEMATICS
OF THE SCHOOL OF SCIENCE AND ENGINEERING OF
TULANE UNIVERSITY
IN PARTIAL FULFILLMENT OF THE REQUIREMENTS
FOR THE DEGREE OF
DOCTOR OF PHILOSOPHY
BY

Zhuolin Qu

Zhuolin Qu

APPROVED: _____

Alexander Kurganov, Ph.D.
CHAIRMAN

_____

Alina Chertock, Ph.D.

_____

Lisa Fauci, Ph.D.

_____

Kun Zhao, Ph.D.

_____

Gustavo Didier, Ph.D.

Abstract

Operator splitting methods have been applied to nonlinear partial differential equations that involve operators of different nature. The main idea of these methods is to decompose a complex equation into simpler sub-equations, which can be solved separately. The main advantage of the operator splitting methods is that they provide a great flexibility in choosing different numerical methods, depending on the feature of each sub-problem. In this dissertation, we have developed highly accurate and efficient numerical methods for several nonlinear partial differential equations, which involve both linear and nonlinear operators.

We first propose a fast explicit operator splitting method for the modified Buckley-Leverett equations which include a third-order mixed derivatives term resulting from the dynamic effects in the pressure difference between the two phases. The method splits the original equation into two equations, one with a nonlinear convective term and the other one with high-order linear terms so that appropriate numerical methods can be applied to each of the split equations: The high-order linear equation is numerically solved using a pseudo-spectral method, while the nonlinear convective equation is integrated using the Godunov-type central-upwind scheme. The spatial order of the central-upwind scheme depends on the order of the piecewise polynomial reconstruction: We test both the second-order minmod-based reconstruction and fifth-order WENO5 one to demonstrate that using higher-order spatial reconstruction leads to more accurate approximation of solutions.

We then propose fast and stable explicit operator splitting methods for two phase-field models (the molecular beam epitaxy equation with slope selection and the Cahn-Hilliard equation), numerical simulations of which require long time computations. The equations are split into nonlinear and linear parts. The nonlinear part is solved using a method of lines combined with an efficient large stability domain explicit ODE solver. The linear part is solved by a pseudo-spectral method, which is based on the exact solution and thus has no stability restriction on the time step size.

We have verified the numerical accuracy of the proposed methods and demonstrated their performance on extensive one- and two-dimensional numerical examples, where different solution profiles can be clearly observed and are consistent with previous analytical studies.

Fast Operator Splitting Methods for Nonlinear PDEs

A DISSERTATION
SUBMITTED ON THE FIFTEENTH DAY OF APRIL, 2016
TO THE DEPARTMENT OF MATHEMATICS
OF THE SCHOOL OF SCIENCE AND ENGINEERING OF
TULANE UNIVERSITY
IN PARTIAL FULFILLMENT OF THE REQUIREMENTS
FOR THE DEGREE OF
DOCTOR OF PHILOSOPHY
BY

Zhuolin Qu

ZHUOLIN QU

APPROVED: _____

ALEXANDER KURGANOV, PH.D.
CHAIRMAN

_____

ALINA CHERTOCK, PH.D.

_____

LISA FAUCI, PH.D.

_____

KUN ZHAO, PH.D.

_____

GUSTAVO DIDIER, PH.D.

Acknowledgement

First and foremost, I would like to express my special gratitude to my advisor Dr. Alexander Kurganov for supporting me in so many ways during these past five years. I really appreciate his contribution of time, ideas and sound advice to make my PhD experience productive and stimulating. The passion and the joy he has with his research has been so contagious and motivational for me that I wish one day I would be a researcher that is as energetic, enthusiastic and hardworking as he is.

I would like to thank my collaborators Dr. Chiu-Yen Kao (Claremont McKenna College) and Dr. Ying Wang (University of Oklahoma) for the collaboration of [1], and Dr. Tao Tang (South University of Science and Technology of China) and Yuanzhen Cheng (Tulane University) for co-authoring [2]. As a researcher at her early stage of career, I really appreciate their great patience and joint-effort, without which the work that presented in this dissertation would not be possible.

I also want to acknowledge Dr. Alina Chertock (North Carolina State University) for the collaboration on the work [3] as well as being in my graduate committee. She has shown me an archetype of a successful women researcher, and from whom I have received generous support during different phases in my pursuit of doctoral degree.

I would like to express my candid gratitude to Dr. Lisa Fauci, Dr. Kun Zhao and Dr. Gustavo Didier for taking time to serve on my committee and give valuable suggestions.

I am deeply indebted to the faculty the Department of Mathematics, Dr. Michelle Lacey, Dr. Xuefeng Wang, Dr. Dagang Yang, Dr. Oleksandr Gromenko, Dr. Tai Ha, Dr. Mahir Can and many others who have shown great generosity and helped me consciously or unconsciously.

I am particular grateful to Dr. James Mac Hyman, who shows continuous support and care in the development of young researchers like me. I have truly enjoyed and benefitted significantly from his inspiring lectures and discussions, which offer me with a great variety of insights in different fields of mathematics.

My special thanks also go to Dr. Tewodros Amdeberhan, who is both a great mentor and a genuine friend of mine. He has been my best role model for a good teacher upon my first semester in Tulane. His enthusiasm and love for teaching has impacted me so much on holding my own ethic to be a good educator. I also greatly appreciate his sound advice and encouragement at various turning points during these five years of my life, which have enabled me to keep my morale up.

I am thankful to the staff members Mrs. Geralyn Caradona, Mrs. Pamela Philastre and Mr. Mark Brown for their help and advice during the day-to-day graduate study.

It would be super hard to get through and stay sane in the graduate school without my fellow peers. I am very appreciative to Shanshan Jiang, Dr. Lu Lu, Dr. Shumo Cui, and Dr. Huicong Li for their altruistic help in numerous aspects of my study and life. Thanks to Yuanzhen Cheng, Lin Jiu, Kui Zhang, Xiao Guan, Asma Azizi (Soodeh) and so on for their company and support during my stay in Tulane. In particular, I want to thank my dear Tong Wu for his constant and selfless support in countless ways.

Finally, I would like to sincerely dedicate this dissertation to my parents, who believed in my capability and have consistently offered their unconditional support.

List of Tables

List of Figures

Contents

Chapter 1

Introduction

In this dissertation, we study the numerical methods for solving nonlinear partial differential equations that arise in various applications and describe a wide range of physical systems, ranging from the epitaxial decomposition of thin film to multi-phase flow in oil reservoirs. In particular, we consider the differential equations which, in the one-dimensional (1-D) case, take the form:

$$u_t = \mathcal{N}u + \mathcal{L}u, \tag{1.1}$$

where u is the variable of interest, $\mathcal{N}$ is a nonlinear differential operator and $\mathcal{L}$ is a linear differential operator.

Computing numerical solutions of equation (1.1) is an important and challenging problem, especially in the case when high-order derivative terms present in the linear operator $\mathcal{L}$ and strong nonlinearity is embedded in operator $\mathcal{N}$. To obtain accurate numerical solutions, one may first discretize the space variable for the right-hand side (RHS) operators $\mathcal{N}u + \mathcal{L}u$ using high-order finite difference/element/volume schemes, followed by applying high-order ODE solvers to integrate in time. However, numerical computations using such approach may sometimes too costly to achieve a desirable resolution.

A standard approach to solve such type of problem is to use an *operator splitting* or *fractional-step method*. Roughly speaking, we approximate the solution of the full complex problem (1.1) by alternatively solving between two simpler differential equations: the linear equation

$$u_t = \mathcal{L}u \tag{1.2}$$

and the nonlinear one

$$u_t = \mathcal{N}u, \tag{1.3}$$

which can be solved separatively. We denote the *exact* solution operators associated with equations (1.2) and (1.3) by $\mathcal{S}_{\mathcal{L}}$ and $\mathcal{S}_{\mathcal{N}}$, respectively. Next, introducing a (small) splitting step Δt, the solution of the original equation (1.1) (which is assumed to be available at time t) is evolved using one of the following splitting methods:

- Lie splitting (first-order sequential splitting) [4]:

$$\begin{aligned} u(x,t+\Delta t) &= \mathcal{S}_{\mathcal{N}}(\Delta t)\,\mathcal{S}_{\mathcal{L}}(\Delta t)\,u(x,t) + \mathcal{O}((\Delta t)^2) \quad \text{or} \\ u(x,t+\Delta t) &= \mathcal{S}_{\mathcal{L}}(\Delta t)\,\mathcal{S}_{\mathcal{S}}(\Delta t)\,u(x,t) + \mathcal{O}((\Delta t)^2), \end{aligned}$$

- Strang splitting (second-order) [5–7]:

$$\begin{aligned} u(x,t+\Delta t) &= \mathcal{S}_{\mathcal{N}}\left(\frac{\Delta t}{2}\right)\mathcal{S}_{\mathcal{L}}(\Delta t)\,\mathcal{S}_{\mathcal{N}}\left(\frac{\Delta t}{2}\right)u(x,t) + \mathcal{O}((\Delta t)^3) \quad \text{or} \\ u(x,t+\Delta t) &= \mathcal{S}_{\mathcal{L}}\left(\frac{\Delta t}{2}\right)\mathcal{S}_{\mathcal{N}}(\Delta t)\,\mathcal{S}_{\mathcal{L}}\left(\frac{\Delta t}{2}\right)u(x,t) + \mathcal{O}((\Delta t)^3), \end{aligned} \tag{1.4}$$

and higher-order splitting methods are proved to involve at least one backward time step size in order to achieve order greater than two [8,9], which may cause numerical instability for time irreversible problems. Thus, to bypass the order-barrier, one may either use a linear combination of the low-order splitting methods such as

- Third order splitting [10]:

$$u(x,t+\Delta t) = \frac{2}{3}\left(\mathcal{S}_{\mathcal{N}}\left(\frac{\Delta t}{2}\right)\mathcal{S}_{\mathcal{L}}\left(\Delta t\right)\mathcal{S}_{\mathcal{N}}\left(\frac{\Delta t}{2}\right)+\mathcal{S}_{\mathcal{L}}\left(\frac{\Delta t}{2}\right)\mathcal{S}_{\mathcal{N}}\left(\Delta t\right)\mathcal{S}_{\mathcal{L}}\left(\frac{\Delta t}{2}\right)\right) - \frac{1}{6}\left(\mathcal{S}_{\mathcal{N}}\left(\Delta t\right)\mathcal{S}_{\mathcal{L}}\left(\Delta t\right)+\mathcal{S}_{\mathcal{L}}\left(\Delta t\right)\mathcal{S}_{\mathcal{S}}\left(\Delta t\right)\right)u(x,t)+\mathcal{O}((\Delta t)^4)$$

(see also [11]) or use the splitting methods containing complex time step size with positive real parts, which have been systematically developed in [12–17]. In this dissertation, we use the second-order Strang splitting method (1.4).

In practice, to implement the splitting method, the exact solution operators $\mathcal{S}_{\mathcal{L}}$ and $\mathcal{S}_{\mathcal{N}}$ are to be substituted by their numerical approximations. Note that the linear (1.2) and nonlinear (1.3) subproblems are of different nature. Therefore, as a main advantage of the operator splitting technique, appropriate high-resolution numerical methods can be applied to each of the split problem.

The operator splitting technique has been successfully applied in the context of convection-diffusion equations, which is a classical equation of the form (1.1) and in 1-D case, it reads as

$$u_t + f(u)_x = \varepsilon u_{xx}. \tag{1.5}$$

Here, u is an unknown variable of interest, f is a nonlinear convection flux and $\varepsilon > 0$ is the diffusion coefficient. To design an accurate and efficient numerical method for the convection diffusion equation (1.5), especially in the convection-dominated case, one needs to overcome the difficulty of keeping the balance between the convection and diffusion terms: many schemes either have extensive numerical viscosity, which makes the solution under-resolved, or introduce spurious oscillations near sharp shock profiles. To numerically preserve this delicate balance, fast explicit operator splitting (FEOS) methods were proposed in [18–21] (see also [22]), where equation

(1.5) was decoupled into a nonlinear hyperbolic equation

$$u_t + f(u)_x = 0 \tag{1.6}$$

and a linear parabolic equation

$$u_t = \varepsilon u_{xx}. \tag{1.7}$$

The corresponding exact solution operators $\mathcal{S}_{\mathcal{N}}$ and $\mathcal{S}_{\mathcal{L}}$ were then replaced by their numerical approximations.

As the main advantage of operator splitting methods, there is great flexibility in choosing different numerical methods for both parts, depending on the nature of subproblems. Equation (1.6) with the nonlinear flux function $f(u)$ is a hyperbolic system of conservation law, and it admits non-smooth solutions (shocks and rarefaction waves), even when a smooth initial condition is prescribed. A wide variety of shock capturing methods have been designed to accurately capture the ensuing non-smooth waves, see, e.g., the monographs [23–28] and reference therein. For the problem at hand, a finite-volume based hyperbolic solver seems to be a natural choice and in particular, the second-order Godunov-type central-upwind schemes [29–31] are attractive options, because they are simple, robust, Riemann-problem-solver-free, yet high-resolution methods and can be used as as "black-box" solvers for general (multidimensional) hyperbolic systems of conservation laws. For the parabolic linear equation (1.7), several efficient numerical methods can be designed. First, it can be reduced to a system of ODEs using the method-of-line technique and then integrated by appropriate ODE solvers: implicit one like [32, 33], explicit ones with large stability domain [34–37], or implicit-explicit one as [32, 38]. Another possibility is to solve (1.7) (practically) exactly using the heat kernel to evolve the intermediate solution at each linear splitting step as it was proposed in [19–21]. A third approach is to employ the pseudo-spectral framework.

In all of these cases, there is no enforced stability restriction on the size of the linear step, hence, large splitting time steps can be made without destabilize the algorithm. As it has been pointed out in [22], the pseudo-spectral method may be especially advantageous when dealing with periodic boundary conditions, since when it comes to numerically implementations, one can take the advantage of the FFT algorithm to significantly increase the efficiency of the algorithms. Notice that, due to the CFL condition, the time step used by the finite-volume methods in the nonlinear part may be smaller than $\Delta t/2$ (where Δt is the splitting time step size in (1.4)). In this case, several nonlinear steps are taken within in one splitting step.

In this dissertation, our goal is to develop highly accurate and efficient numerical methods for several nonlinear PDEs, including modified Buckley-Leverett (MBL) equation and two phase-field models: the molecular beam epitaxy (MBE) equation with slope selection and the Cahn-Hilliard (CH) equation. The main approach is based on the aforementioned FEOS methods. Due to the distinct nature of the associated nonlinear parts, we construct different sets of numerical schemes, which are outlined separately in the following two sections.

1.1 Modified Buckley-Leverett Equation

The first nonlinear PDE that we consider in this dissertation is MBL equation.

The classical Buckley-Leverett (BL) equation was firstly proposed to describe two-phase fluid flow in porous media such as the secondary oil recovery by water injection in oil reservoir. In the 1-D case, the classical BL equation is a scalar conversation law:

$$u_t + F(u)_x = 0,$$

with the flux function $F(u) = f(u)$ defined as

$$f(u) = \begin{cases} 0, & u < 0, \\ \dfrac{u^2}{u^2 + M(1-u)^2}, & 0 \le u \le 1, \\ 1, & u > 1. \end{cases} \tag{1.8}$$

In this model, u denotes the water saturation, f is water fractional flow rate function and M is the viscosity ratio between water and oil. When a gravitational effect is taken into account, then a modified flux $F(u) = g(u)$, where

$$g(u) = f(u)(1 - C(1-u)^2), \tag{1.9}$$

and C is a positive constant, should be used. It is well-known that the entropy solution of the Riemann initial value problem preserves the monotonicity of the initial data. However, the experiments of two-phase flow in porous medium reveal complex overshoot behavior, and the water saturation may develop nonmonotone profiles even with the initial data being monotone. This suggests that a more accurate model is needed to capture such phenomenon.

The MBL equation was then derived, where a third-order mixed derivatives term is included to describe the dynamic capillary pressure. In the 1-D case, the MBL equation reads:

$$u_t + F(u)_x = \varepsilon u_{xx} + \varepsilon^2 \tau u_{xxt}, \quad \varepsilon > 0,\ \tau > 0, \tag{1.10}$$

where F is given by either (1.8) or (1.9). This equation is of pseudo-parabolic type. The existence condition for traveling wave solutions which violate the Oleinik entropy condition, that is, the so-called nonclassical solutions, is reviewed in Chapter 2.

To numerically capture solutions of both the classical BL and MBL equations, one has to deal with the difficulties relate to the presence of high-order derivatives term on the RHS of (1.10). As it has been discussed before, explicit methods using direct finite-difference discretization may be inefficient and a fine mesh is needed to achieve high accuracy and resolve the details in the nonmonotone solution profile. Moreover, additional difficulties are related to the fact that the fluxes (1.8) and (1.9) are nonconvex, and solutions of nonconvex conservation laws computed by high-order methods may fail to converge the physical relevant solution, the entropy solution.

Several numerical methods have been proposed in the literature: First-order finite difference schemes was presented in [39] for BL equation; Second- and third-order Godunov-type staggered central schemes were developed in [40, 41] to capture the nonclassical solutions of the 1-D MBL. In Chapter 2, we introduce a highly accurate and efficient method for (1.10) and then to extend it to a more numerically demanding 2-D case. We follow the idea of FEOS methods and split the MBL equation (1.10) into two simpler equations: the linear equation

$$u_t = \varepsilon u_{xx} + \varepsilon^2 \tau u_{xxt} \tag{1.11}$$

and the nonlinear one

$$(u - \varepsilon^2 \tau u_{xx})_t + F(u)_x = 0. \tag{1.12}$$

We then solve the exact solution operator associated with the high-order linear equation (1.11) using a pseudo-spectral framework, while the nonlinear convective equation (1.12) is integrated using the Godunov-type central-upwind scheme. The spatial order of the central-upwind scheme hinges on the order of the piecewise polynomial reconstruction, hence to achieve high resolution, we apply both the second-order minmod-based reconstruction as well as the fifth-order WENO5 one.

We test the performance of the FEOS method on a number of 1-D and 2-D numerical examples, and the numerical results clearly demonstrate that the use of the higher-order spatial reconstruction leads to substantially higher resolution of nonclassical solutions. While the results obtained using the minmod-based piecewise linear reconstruction are comparable to those reported in [40, 41], the proposed method combined with the fifth-order WENO5 reconstruction outperforms its counterparts as it is clearly demonstrated in our 1-D numerical experiments.

The detailed descriptions of the FEOS methods for MBL equation are given in Chapter 2.

1.2 Phase-Field Models

The second type of nonlinear PDEs that we study in this dissertation involves two equations within the family of phase-field models. The phase field models were originally introduced to describe the interfacial phenomena, and there are two models have attracted much attention: the molecular beam epitaxy (MBE) equation with slope selection and the Cahn-Hilliard (CH) equation.

MBE equation with slope selection models the thin film epitaxy process, in which molecular beams are deposited onto a crystalline substrate and form a thin epitaxial film. In 1-D case, MBE equation with slope selection reads as

$$u_t - f(u_x)_x = -\delta u_{xxxx}, \quad \delta > 0, \tag{1.13}$$

where u is a scaled height function of epitaxial growth of thin films and $\delta > 0$ is a surface diffusion constant.

CH equation models process of phase separation, in which two components of a mixed fluid spontaneously separate from each other and form continuous domain

separately. In 1-D case, CH equation reads as

$$u_t - f(u)_{xx} = -\delta u_{xxxx}, \quad \delta > 0, \tag{1.14}$$

where u represents the binary concentration of the mixed fluid, and δ estimates the interfacial width across two domains, which serves as a diffusion coefficient.

In this dissertation, we consider

$$f(\varphi) = \varphi|\varphi|^2 - \varphi,$$

for which the two phase-field models (1.13) and (1.14) become

$$u_t = (u_x^3)_x - u_{xx} - \delta u_{xxxx}, \quad \delta > 0, \tag{1.15}$$

and

$$u_t = (u^3)_{xx} - u_{xx} - \delta u_{xxxx}, \quad \delta > 0. \tag{1.16}$$

An important feature of equations (1.15) and (1.16) are that they can be viewed as the gradient flows of the energy functionals

$$E(u) = \int_\Omega \left[\frac{\delta}{2}\left(u_{xx}\right)^2 + \frac{1}{4}\left((u_x)^2 - 1\right)^2\right] dx,$$

and

$$E(u) = \int_\Omega \left[\frac{\delta}{2}\left(u_x\right)^2 + \frac{1}{4}\left(u^2 - 1\right)^2\right] dx,$$

respectively. As it has been shown in [42, 43], both energy functionals obey the energy decay property in time:

$$E(u(t)) \leq E(u(s)), \ \forall t \geq s. \tag{1.17}$$

Development of highly accurate and efficient numerical methods for (1.15) and (1.16) involve difficulties from various aspects. Similar to the convection-diffusion equation (1.5), due to the presence of high-order derivatives on the RHS's, explicit schemes usually suffer severe stability restrictions on the size of time step, and numerical simulations of phase-field models usually require long time computations to attain the steady-states that of interests, thus an efficient and accurate numerical method is desired. What's more, explicit methods may also fail to satisfy the essential energy decay property persisted by the physical system, hence the property of being highly stable is also crucial to the design of a robust method.

In Chapter 3, we develop accurate, efficient and robust explicit methods for both (1.15) and (1.16) subject to the periodic boundary conditions. The general idea is based on the aforesaid FEOS methods.

For MBE equation (1.15), we decompose it into the nonlinear,

$$u_t = (u_x^3)_x, \tag{1.18}$$

and linear,

$$u_t = -u_{xx} - \delta u_{xxxx}, \tag{1.19}$$

parts, and the corresponding energy functionals

$$E_{\mathcal{N}}(u) = \frac{1}{4}\int_{\Omega} (u_x)^4 dx$$

and

$$E_{\mathcal{L}}(u) = \int_{\Omega} \left(\frac{\delta}{2}(u_{xx})^2 - \frac{1}{2}(u_x)^2 + \frac{1}{4}\right) dx$$

also follow the energy decay principle (1.17). We then introduce a proper splitting time step and at each splitting step Δt, and the solutions are evolved using Strang splitting method (1.4), where $\mathcal{S}_{\mathcal{N}}$ and $\mathcal{S}_{\mathcal{L}}$ are exact solution operators associated

with equation (1.18) and (1.19), respectively. Similarly, for CH model, we divide the equation (1.16) into two parts and obtain the same linear part (equation (1.19)) and the nonlinear part

$$u_t = (u^3)_{xx}. \tag{1.20}$$

We also have the associated energy functions,

$$E_{\mathcal{N}}(u) = \frac{1}{4}\int_{\Omega} u^4 dx$$

and

$$E_{\mathcal{L}}(u) = \int_{\Omega} \left(\frac{\delta}{2}(u_x)^2 - \frac{1}{2}u^2 + \frac{1}{4}\right) dx$$

decay.

In order to implement the splitting method (1.4), we need to approximate the solution operators $\mathcal{S}_{\mathcal{N}}$ and $\mathcal{S}_{\mathcal{L}}$, which are of diverse attributes and can be integrated by two different numerical methods: The nonlinear subproblems (1.18) and (1.20) are firstly semi-discretized using finite difference schemes in spacial variables and then integrated in time using a large stability domain explicit ODE solver called DUMKA3, in which a step size control mechanism is implemented to largely increase the efficiency of the solver. For the common linear subproblem (1.19), we apply the accurate pseudo-spectral method over the entire splitting time step Δt. Additionally, since the efficiency of splitting methods hinges on the size of its splitting time step, therefore to practically achieve high efficiency, we propose a roughness-dependent adaptive splitting time-stepping strategy, such that the quick phase transitions can be accurately captured using a small splitting time step but a large splitting time step is enabled at other times, especially when the solution is close to its steady state. We demonstrate the performance of the proposed methods on a number of 1-D and 2-D numerical examples, where different stages of phase

motions can be clearly observed.

Chapter 2

A Fast Explicit Operator Splitting Method for Modified Buckley-Leverett Equations

In this chapter, we propose a fast explicit operator splitting method to solve the modified Buckley-Leverett equations which include a third-order mixed derivatives term resulting from the dynamic effects in the pressure difference between the two phases. The method splits the original equation into two equations, one with a nonlinear convective term and the other one with high-order linear terms so that appropriate numerical methods can be applied to each of the split equations: The high-order linear equation is numerically solved using a pseudo-spectral method, while the nonlinear convective equation is integrated using the Godunov-type central-upwind scheme. The spatial order of the central-upwind scheme depends on the order of the piecewise polynomial reconstruction: We test both the second-order minmod-based reconstruction and fifth-order WENO5 one to demonstrate that using higher-order spatial reconstruction leads to more accurate approximation of solutions. A variety of numerical examples in both one and two space dimensions

show that the solutions may have many different saturation profiles depending on the initial conditions, diffusion parameter, and the third-order mixed derivatives parameter. The results are consistent with the study of traveling wave solutions and their bifurcation diagrams.

2.1 Introduction

The Buckley-Leverett (BL) equation was proposed in [44] to describe two-phase fluid flow in porous media. In particular, the BL equation is used to model the secondary oil recovery by water injection in oil reservoir. In the one-dimensional (1-D) case, the classical BL equation is a scalar conversation law:

$$u_t + F(u)_x = 0, \tag{2.1}$$

with the flux function $F(u) = f(u)$ defined as

$$f(u) = \begin{cases} 0, & u < 0, \\ \dfrac{u^2}{u^2 + M(1-u)^2}, & 0 \leq u \leq 1, \\ 1, & u > 1. \end{cases} \tag{2.2}$$

In this model, u denotes the water saturation, f is water fractional flow rate function and M is the viscosity ratio between water and oil. When a gravitational effect is taken into account, then a modified flux $F(u) = g(u)$, where

$$g(u) = f(u)(1 - C(1-u)^2), \tag{2.3}$$

and C is a positive constant, should be used.

Practically relevant initial data for the BL equation (2.1) are Riemann data:

$$u(x,0) = \begin{cases} u_B, & x \leq 0, \\ 0, & x > 0, \end{cases} \tag{2.4}$$

where u_B is a positive constant representing an initial water saturation in the fluid injected into the oil reservoir. It is well-known that the entropy solution of the initial value problem (IVP) (2.1)–(2.4) preserves the monotonicity of the initial data. However, the experiments [45, Figure 5] of two-phase flow in porous medium reveal complex infiltration profiles, which may involve an overshoot, that is, the water saturation may develop nonmonotone profiles even with the initial data being monotone. This suggests that the classical BL equation (2.1) needs to be modified.

In [46–48], the dynamic capillary pressure is introduced to derive the modified Buckley-Leverett (MBL) equation which includes a third-order mixed derivatives term (see §2.2). In the 1-D case, the MBL equation reads:

$$u_t + F(u)_x = \varepsilon u_{xx} + \varepsilon^2 \tau u_{xxt}, \quad \varepsilon > 0,\ \tau > 0, \tag{2.5}$$

where F is given by either (2.2) or (2.3). This equation is of pseudo-parabolic type. The existence condition for traveling wave solutions which violate the Oleinik entropy condition, that is, the so-called nonclassical solutions of (2.5) is discussed in [39]. The phase plane analysis is performed in [49] to study the properties of the traveling waves corresponding to undercompressive shocks. In [40], the finite domain and half-line problem are compared: The solution of the finite domain $[0, L]$ problem converges to that of the half-line $[0, \infty)$ problem exponentially fast as $L \to \infty$ in the sense of a weighted H^1-norm. Therefore, it provides justification to use the numerical solution on the finite domain to approximate the solution of the half-line problem.

When capturing solutions of both the classical BL and MBL equations numerically, one has to deal with the difficulties related to the fact that the fluxes (2.2) and (2.3) are nonconvex. As it was demonstrated in [50], solutions of nonconvex (systems of) conservation laws computed by high-order methods may fail to resolve composite waves and thus may fail to converge to the entropy solution. To overcome this difficulty, a simple adaptive strategy was proposed in [50]: A more diffusive version of the scheme has to be applied near the flux inflection points (this is achieved by using a more diffusive nonlinear limiter there). When the MBL equation is integrated numerically, an additional difficulty is related to the presence of high-order terms on the right-hand side (RHS) of (2.5): It is well-known that in this case, explicit methods may be inefficient especially when a fine mesh is used to accurately capture small scale details of the solution.

Several numerical methods for the MBL equation have been proposed. In [39], a first order finite difference scheme was presented. A more accurate approach has been advocated in [40, 41], where second- and third-order Godunov-type staggered central schemes were developed to capture the nonclassical solutions of the 1-D MBL equation (2.5).

The main goal of this chapter is to develop a highly accurate and efficient method for (2.5) and then to extend it to a more numerically demanding 2-D case. Our approach is based on the fast explicit operator splitting method proposed in [20, 22, 51] to efficiently solve (systems of) convection-diffusion equations and incompressible Navier-Stokes equations.

The main idea of our method is to split the MBL equation (2.5) into two simpler equations: the nonlinear equation

$$(u - \varepsilon^2 \tau u_{xx})_t + F(u)_x = 0 \tag{2.6}$$

and the linear one:

$$u_t = \varepsilon u_{xx} + \varepsilon^2 \tau u_{xxt}. \tag{2.7}$$

We then solve the convection-type equation (2.6) using the Godunov-type central-upwind scheme [29, 30], while the high-order linear equation (2.7) is integrated exactly using a pseudo-spectral framework as it was done in [22, Section 4]. The order of the central-upwind schemes is determined by the order of the piecewise polynomial reconstruction (see, e.g., [29, 30]). We use both the second-order minmod-based piecewise linear and the fifth-order WENO5 reconstructions and demonstrate that the use of the higher-order spatial reconstruction leads to substantially higher resolution of nonclassical solutions. While the results obtained using the minmod-based piecewise linear reconstruction are comparable to those reported in [40, 41], the proposed method combined with the fifth-order WENO5 reconstruction outperforms its counterparts as it is clearly demonstrated in our 1-D numerical experiments.

The organization of this chapter is as follows. In Section 2.2, we revisit the 1-D MBL equation and derive the 2-D MBL equation. In Section 2.3, a fast explicit operator splitting method for both 1-D and 2-D MBL equations is introduced. Numerical accuracy verification of the proposed method is provided Section 2.4, where the performance of the fast explicit operator splitting method is tested on a number of 1-D and 2-D numerical examples.

2.2 Backgrounds

In this section, we re-derive the 1-D MBL equation (the Hassanizadeh-Gray model) and extend it to the 2-D case. We also discuss a classification of different types of solutions of the Riemann problem (2.5), (2.4).

2.2.1 One-Dimensional MBL Equation

Consider the two-phase water-oil flow in an isotropic and homogeneous porous medium. Let S_i $(i = \mathrm{o}, \mathrm{w})$ be the saturations of the oil and water phases, respectively. Then the conservation of mass yields

$$\phi \frac{\partial S_i}{\partial t} + \frac{\partial q_i}{\partial x} = 0, \qquad i = \mathrm{o}, \mathrm{w}, \tag{2.8}$$

where q_i denotes the specific discharge of oil/water and ϕ denotes the porosity of the medium. By Darcy's law [52], q_i is proportional to the gradient of the phase pressure P_i :

$$q_i = -k \frac{k_{ri}(S_i)}{\mu_i} \frac{\partial P_i}{\partial x}, \qquad i = \mathrm{o}, \mathrm{w}, \tag{2.9}$$

where k denotes the absolute permeability, $k_{r\mathrm{o}}$ and $k_{r\mathrm{w}}$ stand for the relative permeabilities of oil and water, respectively, and μ_o and μ_w denote their viscosities. The capillary pressure P_c defines the difference in the pressures of the two phases:

$$P_c = P_\mathrm{o} - P_\mathrm{w}.$$

In [46–48], the dynamic capillary pressure was defined as

$$P_c = p_c(S_\mathrm{w}) - \phi\tau \frac{\partial S_\mathrm{w}}{\partial t}, \tag{2.10}$$

where $p_c(S_\mathrm{w})$ is the *static* capillary pressure, τ is a positive constant and $\frac{\partial S_\mathrm{w}}{\partial t}$ is the dynamic effects. Assume that the medium is completely saturated, that is,

$$S_\mathrm{o} + S_\mathrm{w} = 1. \tag{2.11}$$

Combining (2.8)–(2.11), a general form of the MBL equation is (see [39, 40, 53] for details)

$$\frac{\partial u}{\partial t} + \frac{\partial F(u)}{\partial x} = -\frac{\partial}{\partial x}\left\{H(u)\frac{\partial}{\partial x}\left(J(u) - \tau\frac{\partial u}{\partial t}\right)\right\}, \tag{2.12}$$

where $u = S_{\mathrm{w}}$ is the saturation of water, and F, H, J are functions of u; the flux function F is equal to either f given by (2.2) or g given by (2.3).

In this chapter, we consider the MBL equation (2.5), which is a version of (2.12) with the linearized RHS, obtained by taking

$$H(u) = \varepsilon^2 \quad \text{and} \quad J(u) = -\frac{u}{\varepsilon},$$

see [39, 40, 53].

2.2.2 Two-Dimensional MBL Equation

In this section, we extend the 1-D MBL equation to its 2-D version (the 2-D BL equation was derived in [54], also see [55]).

If we consider the flow where imbibition takes places under influence of gravity [56], then the mass balance gives

$$\phi\frac{\partial(\rho_i S_i)}{\partial t} + \nabla\cdot(\rho_i \boldsymbol{q}_i) = 0, \qquad i = \mathrm{o}, \mathrm{w},$$

where ρ_{o} and ρ_{w} denote the density of oil and water phases, both of which are considered to be incompressible, so

$$\phi\frac{\partial S_i}{\partial t} + \nabla\cdot(\boldsymbol{q}_i) = 0, \qquad i = \mathrm{o}, \mathrm{w}. \tag{2.13}$$

We again assume that the medium is completely saturated, that is, (2.11) is

satisfied. This, in turn, gives

$$\nabla \cdot (\boldsymbol{q}_{\mathrm{o}} + \boldsymbol{q}_{\mathrm{w}}) = \nabla \cdot \boldsymbol{q} = 0. \tag{2.14}$$

Throughout this chapter, we assume that $\boldsymbol{q} = \text{Const}$.

By Darcy's law, the momentum balance equation is

$$\boldsymbol{q}_i = \lambda_i(\nabla P_i + \rho_i \tilde{g} \boldsymbol{e}_z), \tag{2.15}$$

where

$$\lambda_i = -k \frac{k_{r_i}(S_i)}{\mu_i}, \tag{2.16}$$

$\tilde{g}$ is a gravitational constant and $\boldsymbol{e}_z$ is a unit vector in the z-direction.

Combining (2.13)–(2.15) with the same capillary pressure formulation (2.10), which was used in the 1-D case, the following model is obtained:

$$u_t + \nabla \cdot \left[f(u) \frac{\boldsymbol{q}}{\phi} - f(u)(1-u)^2 \frac{k(\rho_{\mathrm{w}} - \rho_{\mathrm{o}})\tilde{g}}{\mu_{\mathrm{o}}\phi} \boldsymbol{e}_z \right] = -\nabla \cdot \left[H(u) \nabla (J(u) - \tau u_t) \right], \tag{2.17}$$

where f is given by (2.2) with $M = \mu_{\mathrm{w}}/\mu_{\mathrm{o}}$,

$$H(u) = \frac{k}{\mu_{\mathrm{o}}} f(u)(1-u)^2 \quad \text{and} \quad J(u) = \frac{p_c(u)}{\phi}.$$

This is a general form of the 2-D MBL equation, which can be rewritten as follows. We use $\boldsymbol{q} = (q_1, q_2)^T$ to rescale the space variables,

$$x \frac{\phi}{q_1} \to x, \quad z \frac{\phi}{q_2} \to z,$$

take $\phi = \mathcal{O}(\varepsilon)$, and denote

$$M := \frac{\mu_{\mathrm{w}}}{\mu_{\mathrm{o}}}, \qquad C := \frac{k(\rho_{\mathrm{w}} - \rho_{\mathrm{o}})\tilde{g}}{\mu_{\mathrm{o}} q_2}.$$

Then, equation (2.17) reduces to

$$u_t + \nabla \cdot [f(u)(1,1)^T - Cf(u)(1-u)^2 \boldsymbol{e}_z] = \varepsilon \Delta u + \varepsilon^2 \tau \Delta u_t,$$

which can be rewritten as

$$u_t + F(u)_x + G(u)_z = \varepsilon \Delta u + \varepsilon^2 \tau \Delta u_t \tag{2.18}$$

where $F(u) = f(u)$ and $G(u) = g(u)$ are given by (2.2) and (2.3), respectively. This equation is a modification of the classical 2-D BL equation

$$u_t + F(u)_x + G(u)_z = 0, \tag{2.19}$$

when the capillary pressure in (2.10) is taken to be constant.

2.2.3 Bifurcation Diagram

Our goal is to understand the nature of solutions of the Riemann problem (2.5), (2.4) for different values of the initial parameter u_B. To this end, we follow [39] and study the traveling wave solutions of (2.5).

For $\tau > 0$, we look for a traveling wave solution $u(\eta)$, where $\eta = (x - st)/\varepsilon$. Substituting $u(\eta)$ into (2.5) results in the following ODE:

$$-su' + (F(u))' = u'' - s\tau u'''. \tag{2.20}$$

This equation is to be solved subject to the boundary conditions at infinities,

$$u(-\infty) = u_B, \quad u(\infty) = 0, \tag{2.21}$$

which together with the Rankine-Hugoniot condition determine the traveling wave speed:

$$s = \frac{F(u_B) - F(0)}{u_B - 0} = \frac{F(u_B)}{u_B}.$$

We then integrate equation (2.20) over (η, ∞) and reduce the order by one:

$$-su + F(u) = u' - s\tau u''. \tag{2.22}$$

It was proved in [39] that existence of the traveling wave solution satisfying (2.22), (2.21) depends on the parameter τ in the following manner. There exists a critical value τ_F^* such that for all $\tau \in [0, \tau_F^*]$, there exists a solution of (2.22), (2.21) with $u_B = \alpha_F$, where α_F is the unique root of the equation

$$F'(u) = \frac{F(u)}{u}.$$

For $\tau > \tau_F^*$, there exists a unique value of $\widetilde{u} > \alpha_F$ such that the solution of the boundary value problem (BVP) (2.22), (2.21) with $u_B = \widetilde{u}$ exists. For $u_B < \widetilde{u}$, the solution of (2.22), (2.21) will exist only if $u_B < \underset{\sim}{u}$, where $\underset{\sim}{u}$ is the unique root of the following equation:

$$F(r) - \frac{F(\widetilde{u})}{\widetilde{u}}\, r = 0, \quad 0 < r < \widetilde{u}. \tag{2.23}$$

For a given τ, the values of $\widetilde{u}$ and $\underset{\sim}{u}$ can be found as follows. Since the traveling wave (when exists) is a decreasing function of η, we perform the following change of

variables: $z(u) = -u'(\eta(u))$, which transforms equation (2.22) into

$$s\tau z z' + z = su - F(u), \quad u \in (0, u_B). \tag{2.24}$$

Since we have assumed that $u(\eta)$ is decreasing, $z(u) > 0$ for all $u \in (0, u_B)$. Moreover,

$$z(0) = z(u_B) = 0. \tag{2.25}$$

We therefore need to find $u_B > \alpha_F$ satisfying the above conditions. This can be done by applying a shooting method to the BVP (2.24), (2.25), and the obtained u_B is the desired value of $\widetilde{u}$. After this, we can find the corresponding value of $\underset{\sim}{u}$ by (numerically) solving equation (2.23).

We now take particular examples of $F = f$ given by (2.2) and $F = g$ given by (2.3) with $M = 1/2$ and $C = 2$ and numerically compute α_f, α_g, τ_f^*, τ_g^*, and the values of $\widetilde{u}$ and $\underset{\sim}{u}$ for τ uniformly distributed in the interval $[0, 5]$. The obtained results are summarized in the bifurcation diagram shown in Figure 2.1. Notice that when $\tau \leq \tau^*$, both $\widetilde{u}$ and $\underset{\sim}{u}$ are equal to α.

Based on the bifurcation diagram in Figure 2.1, three qualitatively different types of solution profiles of the Riemann problem (2.5), (2.4) are possible (all of them are illustrated in the numerical examples presented in Section 2.4):

(i) If $u_B > \widetilde{u}$, then the left state u_B is connected to $\widetilde{u}$ through a rarefaction wave, followed by a shock that jumps from $\widetilde{u}$ down to 0;

(ii) If $\underset{\sim}{u} < u_B < \widetilde{u}$, then the solution jumps up from u_B to $\widetilde{u}$ through a shock, and then jumps down from $\widetilde{u}$ to 0 through another shock;

(iii) If $u_B < \underset{\sim}{u}$, then the solution consists of a single shock that connects u_B with 0.

Remark 2.2.1 Notice that nonclassical solutions of the Riemann problem (2.5), (2.4) will correspond to nonmonotone solutions of the BVP (2.22), (2.21), obtained

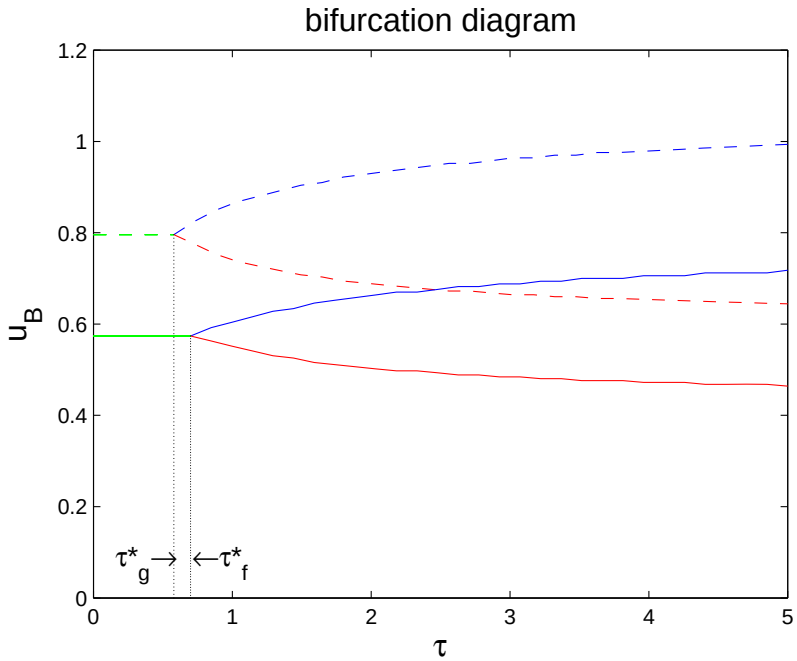

Figure 2.1: Bifurcation diagram in the (τ, u_B)-space for the flux functions f (solid lines) and g (dashed lines). For both f and g, the upper curves represent $\widetilde{u}$ and the lower curves represent $\underset{\sim}{u}$.

in Case (ii) above.

2.3 Fast Explicit Operator Splitting Method

There are many numerical methods for convection-diffusion equations, which arise in a wide variety of applications. However, in the convection dominated case, many schemes either have extensive numerical viscosity, which makes the solution under-resolved, or introduce spurious oscillations near sharp shock profiles. An attempt to preserve a delicate balance between the convection and diffusion terms was made in [19, 20, 22, 51], where a fast explicit operator splitting method was proposed. In this section, we will use the same splitting idea to design new numerical schemes for the MBL equations. For the sake of brevity, we will only present the 1-D method (its extension to the 2-D case is rather straightforward).

2.3.1 Splitting Strategy

To apply splitting methods, we first combine the time derivative terms, that is, we rewrite the MBL equation (2.5) as

$$(u - \varepsilon^2 \tau u_{xx})_t + F(u)_x = \varepsilon u_{xx}. \tag{2.26}$$

We then split equation (2.26) into two simpler equations: the nonlinear convection-type equation

$$(u - \varepsilon^2 \tau u_{xx})_t + F(u)_x = 0 \tag{2.27}$$

and the linear diffusion-type equation

$$(u - \epsilon^2 \tau u_{xx})_t = \varepsilon u_{xx}, \tag{2.28}$$

and denote the *exact* solution operators associated with equations (2.27) and (2.28) by $\mathcal{S}_{\mathcal{N}}$ and $\mathcal{S}_{\mathcal{L}}$, respectively.

Let us assume that at time t, the solution of the original MBL equation (2.26) is available. We then introduce a time step Δt and evolve the solution from t to $t + \Delta t$ using the second-order Strang splitting method:

$$u(x, t + \Delta t) = \mathcal{S}_{\mathcal{N}}\left(\frac{\Delta t}{2}\right) \mathcal{S}_{\mathcal{L}}\left(\Delta t\right) \mathcal{S}_{\mathcal{N}}\left(\frac{\Delta t}{2}\right) u(x, t) + \mathcal{O}((\Delta t)^3).$$

To implement the splitting method in practice, the exact solution operators $\mathcal{S}_{\mathcal{N}}$ and $\mathcal{S}_{\mathcal{L}}$ are to be replaced by their numerical approximations. Our particular choice of the required nonlinear and linear solvers are described in Sections 2.3.2 and 2.3.3, respectively.

2.3.2 Central-Upwind Schemes for Equation (2.27)

In order to develop a numerical method for the nonlinear convection-type equation (2.27), we first introduce an intermediate variable v and rewrite equation (2.27) as a system of two equations:

$$v_t + F(u)_x = 0, \tag{2.29}$$

$$u - \varepsilon^2 \tau u_{xx} = v. \tag{2.30}$$

We then solve equation (2.29) using a semi-discrete finite-volume method. To this end, we introduce a uniform spatial grid $x_\alpha := \alpha \Delta x$, the finite volume cells $I_j := [x_{j-\frac{1}{2}}, x_{j+\frac{1}{2}}]$, and the cell averages

$$\bar{v}_j(t) := \frac{1}{\Delta x} \int\limits_{I_j} v(x,t)\, dx,$$

which are evolved in time by solving the following systems of ODEs:

$$\frac{d}{dt} \bar{v}_j(t) = -\frac{H_{j+\frac{1}{2}}(t) - H_{j-\frac{1}{2}}(t)}{\Delta x}, \tag{2.31}$$

where $H_{j+\frac{1}{2}}$ are numerical fluxes. We use the central-upwind fluxes proposed in [30]:

$$H_{j+\frac{1}{2}}(t) := \frac{a^+_{j+\frac{1}{2}} F(u^-_{j+\frac{1}{2}}) - a^-_{j+\frac{1}{2}} F(u^+_{j+\frac{1}{2}})}{a^+_{j+\frac{1}{2}} - a^-_{j+\frac{1}{2}}} + \frac{a^+_{j+\frac{1}{2}} a^-_{j+\frac{1}{2}}}{a^+_{j+\frac{1}{2}} - a^-_{j+\frac{1}{2}}} \left[u^+_{j+\frac{1}{2}} - u^-_{j+\frac{1}{2}} \right], \tag{2.32}$$

where all of the quantities on the RHS depend on time, but from now on we omit this dependence for the sake of brevity.

In (2.32), $u^\pm_{j+\frac{1}{2}}$ are the right- left-sided point values of the piecewise polynomial reconstruction of u at $x = x_{j+\frac{1}{2}}$. This reconstruction is obtained from the cell averages $\bar{u}_j(t) := \frac{1}{\Delta x} \int_{I_j} u(x,t)\, dx$, which are assumed to be available at time t. A

formal spatial order of the semi-discrete scheme (2.31), (2.32) is determined by the formal order of the reconstruction. In this chapter, we use either a second-order scheme obtained with the help of a generalized minmod-based reconstruction (see [57–60]) or a fifth-order scheme, for which the values of $u^{\pm}_{j+\frac{1}{2}}$ are computed using the WENO5 approach (see, e.g., [61,62]). The right- and left-sided local speeds of propagation, $a^{\pm}_{j+\frac{1}{2}}$, are determined using the following estimates (see [50]):

$$a^{+}_{j+\frac{1}{2}} = \max\Big\{\max_{u\in[m_{j+\frac{1}{2}},M_{j+\frac{1}{2}}]}\{F'(u)\},0\Big\},\quad a^{-}_{j+\frac{1}{2}} = \min\Big\{\min_{u\in[m_{j+\frac{1}{2}},M_{j+\frac{1}{2}}]}\{F'(u)\},0\Big\},$$

where $m_{j+\frac{1}{2}} := \min\{u^{-}_{j+\frac{1}{2}}, u^{+}_{j+\frac{1}{2}}\}$ and $M_{j+\frac{1}{2}} := \max\{u^{-}_{j+\frac{1}{2}}, u^{+}_{j+\frac{1}{2}}\}$.

Finally, a fully discrete scheme for (2.29) is obtained by applying an ODE solver to the ODE system (2.31). In our numerical experiments, we have used the third-order strong stability preserving Runge-Kutta (SSP-RK) method (see [63,64]).

At each stage of SSP-RK method, as long as the new values of v are obtained, the elliptic equation (2.30) is to be solved to update u. Since (2.30) is a linear equation with the periodic boundary conditions, it can be exponentially accurately and efficiently solved using the pseudo-spectral method. To do so, we first use the Fast Fourier Transform (FFT) algorithm to compute the discrete Fourier coefficients $\{\widehat{v}_m\}$ from the cell averages $\{\overline{v}_j\}$ and substitute the Fourier expansions

$$u(x) = \sum_m \widehat{u}_m e^{imx} \quad \text{and} \quad v(x) = \sum_m \widehat{v}_m e^{imx}$$

into (2.30). We then obtain a simple algebraic equation for the discrete Fourier coefficients $\widehat{u}_m$:

$$\widehat{u}_m - \varepsilon^2\tau(ik)^2\widehat{u}_m = \widehat{v}_m,$$

and thus,

$$\widehat{u}_m = \frac{\widehat{v}_m}{1+\varepsilon^2\tau k^2},$$

for all m. At the end, we recover the cell averages $\{\overline{u}_j\}$ from the Fourier coefficients $\{\widehat{u}_m\}$ using the inverse FFT algorithm.

Remark 2.3.1 As it has been mentioned in Section 2.1, the solution computed by a high-order central-upwind scheme may fail to resolve composite waves and thus may not converge to the entropy solution. This was discovered in [50], where a simple adaptive strategy was proposed to overcome this difficulty: A more diffusive nonlinear limiter (the most diffusive minmod limiter [57–60] with the parameter 1) has to be applied near the flux inflection points. We have implemented this adaptive strategy to compute the numerical solutions presented in Section 2.4, but in fact it was not necessary in any of the studied numerical examples. Therefore, in Section 2.4, we present the results obtained by the direct implementation of the central-upwind scheme described here.

2.3.3 Pseudo-Spectral Method for Equation (2.28)

Since equation (2.28) is linear, a pseudo-spectral method would lead to a highly accurate approximation of the solution operator $\mathcal{S}_{\mathcal{L}}$. Similarly to the way equation (2.30) was solved in Section (2.3.2), we first use the FFT algorithm to compute the discrete Fourier coefficients $\{\widehat{u}_m\}$ from the available cell averages $\{\overline{u}_j\}$ and approximate u at time t by its Fourier expansion:

$$u(x,t) \approx \sum_m \widehat{u}_m(t)\, e^{imx}.$$

Substituting this into (2.28) results in the following simple linear ODEs for the discrete Fourier coefficients:

$$\frac{d}{dt}\left[\widehat{u}_m(t) - \varepsilon^2\tau(im)^2\widehat{u}_m\right] = \varepsilon(im)^2\widehat{u}_m,$$

which can be solved exactly on the time interval $(t, t+\Delta t]$ for any Δt:

$$\widehat{u}_m(t+\Delta t) = \exp\left(\frac{-\varepsilon m^2 \Delta t}{1+\varepsilon^2 \tau m^2}\right) \widehat{u}_m(t).$$

Finally, we use the inverse FFT algorithm to obtain the cell averages of the solution at the new time level, $\{\overline{u}_j(t+\Delta t)\}$, out of the set of its discrete Fourier coefficients $\{\widehat{u}_m(t+\Delta t)\}$.

Remark 2.3.2 In this chapter, we restrict our consideration to periodic boundary conditions only. If other boundary conditions are prescribed, the proposed method still applies with the only exception that the FFT and inverse FFT algorithms are to be replaced with the Fast Chebyshev Transform and inverse Fast Chebyshev Transform in the solutions of both equations (2.30) and (2.28).

2.4 Numerical Results

In this section, we test the performance of the proposed fast explicit operator splitting method on several 1-D and 2-D examples. In the 1-D examples, we compare the results obtained by applying the second-order minmod-based reconstruction and the fifth-order WENO5 approach on several different grids to demonstrate that higher-order spatial reconstruction leads to much higher resolution of computed solutions. We also compare the behavior of solutions of equation (2.5) with different nonlinear fluxes (2.2) and (2.3). The obtained results are consistent with the traveling wave results presented in the bifurcation diagrams in Figure 2.1. In the 2-D examples, we only use a more computationally efficient and accurate WENO5 reconstruction.

In all of the examples below, the periodic boundary conditions are imposed, the diffusion coefficient is $\varepsilon = 10^{-3}$, and the minmod parameter $\theta = 1.3$ is chosen. More

precisely, the minmod derivative of a grid function $\{\psi_j\}$ is

$$(\psi_x)_j = \text{minmod}\left(\theta\,\frac{\psi_{j+1}-\psi_j}{\Delta x},\ \frac{\psi_{j+1}-\psi_{j-1}}{2\Delta x},\ \theta\,\frac{\psi_j-\psi_{j-1}}{\Delta x}\right),$$

where the minmod function is defined by

$$\text{minmod}(z_1, z_2, \ldots) := \begin{cases} \min(z_1, z_2, \ldots), & \text{if } \ z_i > 0 \ \ \forall i, \\ \max(z_1, z_2, \ldots), & \text{if } \ z_i < 0 \ \ \forall i, \\ 0, & \text{otherwise.} \end{cases}$$

2.4.1 Linear Accuracy Tests

In this section, we test the accuracy and convergence of the proposed 1-D and 2-D methods by solving the MBL equations (2.5) and (2.18) with the linear fluxes, for which the exact solutions can be easily obtained using the spectral method (to compute the errors reported in Tables 2.1–2.3 below we used the truncated spectral solutions with the number of modes equal to the number of grid cells used to generate the corresponding numerical solutions).

We begin with the 1-D case and consider the following IVP:

$$\begin{cases} u_t + u_x = \varepsilon u_{xx} + 5\varepsilon^2 u_{xxt}, & (x,t) \in (0,2) \times (0,2], \\ u(x,0) = \sin(\pi x), & x \in [0,2]. \end{cases}$$

In Tables 2.1 and 2.2, we show the errors and experimental convergence rates achieved with the second-order minmod-based and fifth-order WENO5 reconstructions, respectively. The errors, measured in both the L^1-, L^2- and L^∞-norms, confirm the expected convergence rates. The second-order minmod-based reconstruction leads to the second-order experimental convergence, while the fifth-order WENO5 reconstruction increase the convergence rate to the

N	L^1-error	rate	L^2-error	rate	L^∞-error	rate
64	1.4755E-02	-	1.3400E-02	-	2.4467E-02	-
128	2.6529E-03	2.4755	2.4454E-03	2.4541	5.9092E-03	2.0498
256	4.5606E-04	2.5403	3.7676E-04	2.6983	9.7694E-04	2.5966
512	1.0240E-04	2.1551	8.0050E-05	2.2347	1.1068E-04	3.1418
1024	2.5122E-05	2.0272	1.9691E-05	2.0233	1.9653E-05	2.4936
2048	6.2732E-06	2.0017	4.9248E-06	1.9994	4.9236E-06	1.9969

Table 2.1: The 1-D linear accuracy test using the minmod-based reconstruction.

N	L^1-error	rate	L^2-error	rate	L^∞-error	rate
64	1.3145E-05	-	1.0293E-05	-	1.0782E-05	-
128	8.6308E-07	3.9289	6.7674E-07	3.9269	6.7037E-07	4.0076
256	8.3592E-08	3.3681	6.5634E-08	3.3661	6.4986E-08	3.3667
512	9.6942E-09	3.1082	7.6128E-09	3.1079	7.5732E-09	3.1012
1024	1.1924E-09	3.0233	9.3638E-10	3.0233	9.3454E-10	3.0186
2048	1.5306E-10	2.9617	1.2021E-10	2.9616	1.2057E-10	2.9544

Table 2.2: The 1-D linear accuracy test using the WENO5 reconstruction.

third one. We would also like to point out that the absolute size of the obtained WENO5 errors is about 3–4 orders of magnitude smaller than the minmod ones.

We note that in the WENO5 case, the convergence rates are limited by the accuracy of the third-order SSP-RK solver and the second-order Strang splitting algorithm. The latter, however, does not affect the obtained rates even for large number of grid cells (N) since the splitting errors are very small thanks to the smallness of the diffusion coefficient ε (according to the error estimates obtained in [20, 22, 51], the splitting error is expected to be proportional to $\varepsilon^3(\Delta t)^2$).

In the 2-D accuracy test, we consider the 2-D IVP,

$$\begin{cases} u_t + u_x + u_y = \varepsilon\Delta u + 5\varepsilon^2(\Delta u)_t, & (x,y) \in (0,2)\times(0,2), \quad t \in (0,2], \\ u(x,y,0) = \sin(\pi x) + \sin(\pi y), & (x,y) \in (0,2)\times(0,2), \end{cases}$$

which is numerically solved using the fast explicit operator splitting method

N	L^1-error	rate	L^2-error	rate	L^∞-error	rate
64×64	3.3396E-05	-	2.0586E-05	-	2.1565E-05	-
128×128	2.1915E-06	3.9297	1.3535E-06	3.9269	1.3407E-06	4.0076
256×256	2.1273E-07	3.3648	1.3127E-07	3.3661	1.2997E-07	3.3667
512×512	2.4679E-08	3.1077	1.5226E-08	3.1079	1.5146E-08	3.1012
1024×1024	3.0370E-09	3.0226	1.8736E-09	3.0226	1.8690E-09	3.0185

Table 2.3: The 2-D linear accuracy test using the WENO5 reconstruction.

utilizing the WENO5 reconstruction. As in the 1-D case, the expected experimental third-order convergence rate is achieved, as one can see in Table 2.3.

2.4.2 Nonlinear Accuracy Test

In this section, we test the accuracy and convergence of the proposed 1-D methods by solving the MBL equation (1.5) with the nonlinear flux.

Consider the following IVP:

$$\begin{cases} u_t + f(u)_x = \varepsilon u_{xx} + 0.2\varepsilon^2 u_{xxt}, & (x,t) \in (0,2) \times (0, 0.125], \\ u(x,0) = 0.45(\sin(\pi x) + 1), & x \in [0,2]. \end{cases}$$

where f is given by (2.2) with $M = 2$. In Tables 2.4 and 2.5, we show the errors and experimental convergence rates achieved with the second-order minmod-based and fifth-order WENO5 reconstructions, respectively. The corresponding reference solutions are obtained by computing the numerical solutions on a very fine grid with $N = 16384$, and the errors are measured in both the L^1-, L^2- and L^∞-norms. Compared with the results obtained with linear flux in Section 2.4.1, the convergence rates here are lower due to the nonlinearity in the flux f and presence of sharp gradient areas in the solution, see Figure 2.2. However, the fifth-order WENO5 reconstruction still leads to slightly higher experimental convergence rates and smaller errors than the second-order minmod-based reconstruction does.

N	L^1-error	rate	L^2-error	rate	L^∞-error	rate
64	5.1709E-03	-	1.1041E-02	-	4.9341E-02	-
128	1.7538E-03	1.5600	5.1379E-03	1.1036	3.5078E-02	0.4922
256	5.3929E-04	1.7013	1.9756E-03	1.3789	1.8171E-02	0.9490
512	1.4631E-04	1.8821	6.1700E-04	1.6790	6.7943E-03	1.4192
1024	3.6482E-05	2.0038	1.6260E-04	1.9239	2.0300E-03	1.7429
2048	8.8589E-06	2.0420	3.9584E-05	2.0383	5.0771E-04	1.9994

Table 2.4: The nonlinear accuracy test using the minmod-based reconstruction.

N	L^1-error	rate	L^2-error	rate	L^∞-error	rate
64	2.8837E-03	-	7.5782E-03	-	4.0485E-02	-
128	8.6877E-04	1.7309	3.1722E-03	1.2564	2.2508E-02	0.8469
256	2.0925E-04	2.0538	9.6753E-04	1.7131	8.8667E-03	1.3440
512	3.9587E-05	2.4021	1.9185E-04	2.3344	2.0925E-03	2.0832
1024	7.7174E-06	2.3588	3.1650E-05	2.5997	3.5922E-04	2.5422
2048	1.7354E-06	2.1529	6.5627E-06	2.2698	6.8772E-05	2.3850

Table 2.5: The nonlinear accuracy test using the WENO5 reconstruction.

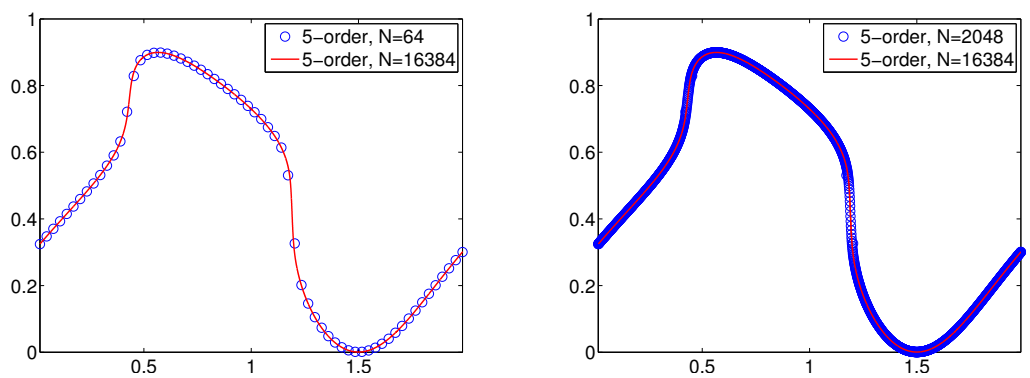

Figure 2.2: Nonlinear Accuracy Test: Solutions computed using the fifth-order WENO5 reconstructions on three different grids at the final time $T = 0.125$.

2.4.3 High-Resolution via the WENO5 Reconstruction

In this section, we show that the use of the fifth-order WENO5 reconstruction leads to much more accurate and efficient method compared with the one that utilizes the second-order minmod-based reconstruction.

We consider the 1-D MBL equation (2.5),(2.2) with the initial condition

$$u(x,0) = \begin{cases} u_B, & \text{if } x \in (0.75, 2.25), \\ 0, & \text{otherwise} \end{cases} \qquad x \in [0,3].$$

We set the parameter M in flux (2.2) to be $M = 1/2$ and compute the solution at the final time $T = 0.5$ for three different sets of values of τ and u_B that correspond to three qualitatively different solutions.

Example 1: $\tau = 3.5$**,** $u_B = 0.85 > \widetilde{u}$

The first pair (τ, u_B) corresponds to Case (i) according to the bifurcation diagram in Figure 2.1, see Section 2.2.3. One can prove that the right part of the exact solution consists of a rarefaction wave for $x \in [2.315, 2.711]$, which is connected to a plateau of height $\widetilde{u} \approx 0.698$, which is then followed by a shock at $x \approx 2.893$.

The solutions computed using both the second- and fifth-order reconstructions are shown in Figure 2.3 (left). To check the accuracy of the obtained solutions, we need to verify how accurate the predicted plateau height is. We therefore zoom in at the plateau area and show the details of the computed solutions in Figure 2.3 (right). As one can see, the plateau height, computed using the WENO5 reconstruction is more accurate even than the plateau height computed using the minmod-based reconstruction on a much finer grid.

Example 2: $\tau = 5$**,** $\underset{\sim}{u} < u_B = 0.66 < \widetilde{u}$

The second pair of (τ, u_B) corresponds to Case (ii) according to the bifurcation diagram in Figure 2.1, see Section 2.2.3. The exact solution is now completely different from the one in Example 1: Its right part consists of a jump up (located at $x \approx 2.597$) to a plateau of height $\widetilde{u} \approx 0.713$ and a jump down (located at $x \approx 2.881$)

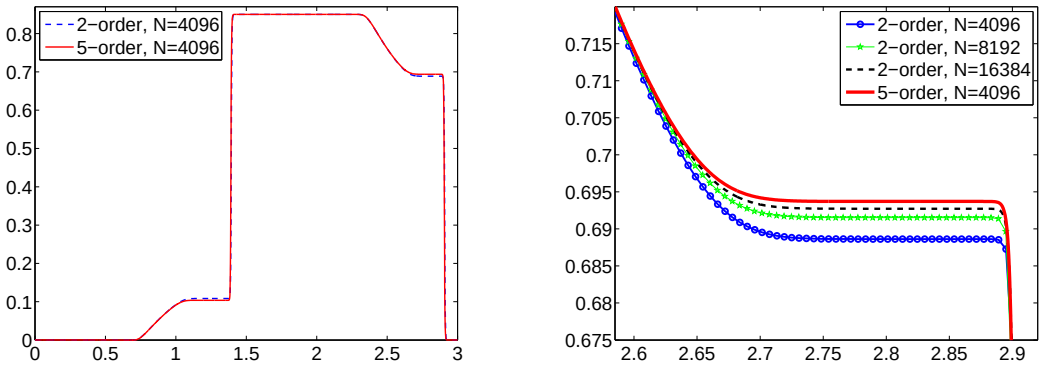

Figure 2.3: Example 1: Solutions computed using the second-order minmod-based and fifth-order WENO5 reconstructions (left); zoom in at the plateau area (right).

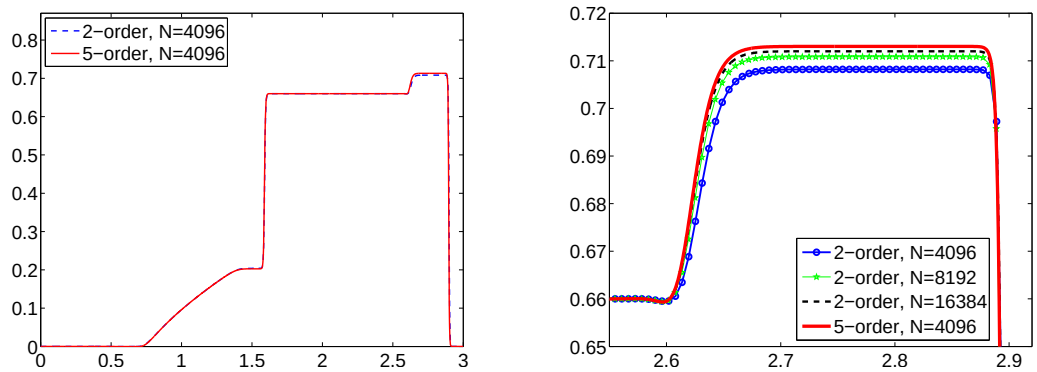

Figure 2.4: Example 2: Solutions computed using the second-order minmod-based and fifth-order WENO5 reconstructions (left); zoom in at the plateau area (right).

to 0. This is a nonclassical (nonmonotone) solution, which is hard to capture since numerical diffusion would typically reduce the height of the newly created plateau. Once again, the use of the WENO5 reconstruction leads to a much more accurate computed solution, see Figure 2.4.

Example 3: $\tau = 5$, $\underset{\sim}{u} < u_B = 0.52 < \widetilde{u}$

In the third example, we take another pair of (τ, u_B), which still corresponds to Case (ii) according to the bifurcation diagram in Figure 2.1, but with a smaller value of u_B, which makes the solution nature to be slightly different. Namely, the connection between the u_B state and the plateau (which still has the same height as in Example 2) is nonmonotone since the exact solution now develops an oscillatory

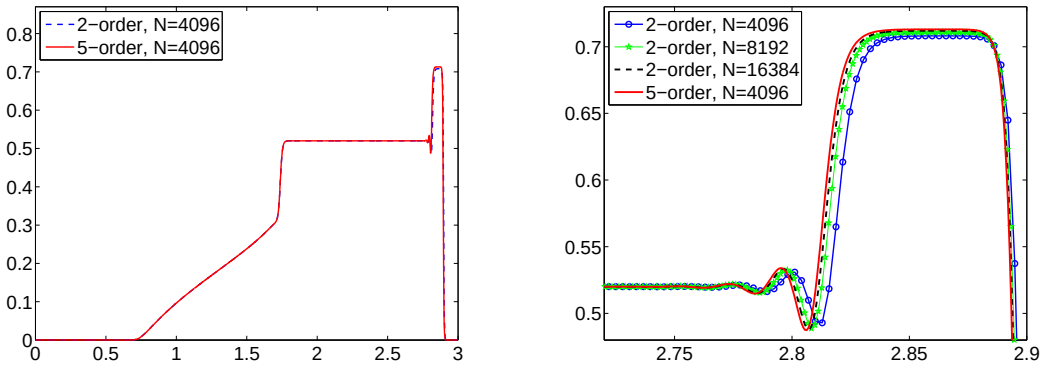

Figure 2.5: Example 3: Solutions computed using the second-order minmod-based and fifth-order WENO5 reconstructions (left); zoom in at the plateau area (right).

part around $x = 2.8$. As in Examples 1 and 2, one can see that the results obtained with the help of the WENO5 reconstruction are more accurate than the minmod results, see Figure 2.5.

Computational Cost

To perform a fair comparison between the two versions of the proposed fast explicit operator splitting method, we compare their CPU times, which are recorded in Table 2.6. As one can see, for a fixed grid, the use of the WENO5 reconstruction increases the computational cost by about 35%. However, it is clear that to achieve the same quality of resolution with the minmod-based reconstruction, one needs to use a substantially finer mesh, which makes the WENO5-based method to be not only more accurate, but also more efficient.

	Example 1		**Example 2**		**Example 3**	
N	minmod	WENO5	minmod	WENO5	minmod	WENO5
1024	1.3572	1.9812	1.3884	2.0124	1.3728	2.0280
2048	5.8656	8.4085	6.3492	8.2525	5.8500	8.4865
4096	25.8494	36.2234	25.8962	35.7398	25.6778	36.0674
8192	112.6483	151.3210	111.6499	151.2274	108.9511	151.9762
16384	476.3802	617.8264	474.6018	630.4156	470.7018	627.5422

Table 2.6: Examples 1–3: Comparison of the CPU times.

$(0.2, 0.85)$	$(0.65, 0.85)$	$(3.5, 0.85)$
$(0.2, 0.68)$	$(0.65, 0.68)$	$(3.5, 0.68)$
$(0.2, 0.55)$	$(0.65, 0.55)$	$(3.5, 0.55)$

Table 2.7: The values of (τ, u_B) pairs used in the nine experiments reported in Figure 2.7.

2.4.4 Numerical Study of the Gravitational Effects

In this section, we study the gravitational effects by comparing the numerical solutions of the MBL equation (2.5) subject to the following initial data:

$$u(x,0) = \begin{cases} u_B, & \text{if } x \in (4,10), \\ 0, & \text{otherwise} \end{cases} \qquad x \in [0,13], \tag{2.33}$$

but with two different fluxes, $F = f$ and $F = g$, given by (2.2) and (2.3), respectively (recall that the g flux is obtained from the f flux when the gravity is taken into account). We take the flux parameters $M = 1/2$ and $C = 2$, and test the behavior of the solutions for nine representative pairs (τ, u_B) given in Table 2.7 and also marked by "$\times$" signs in Figure 2.6. The solutions obtained by the fast explicit operator splitting method using the fifth-order WENO5 reconstruction are shown in Figure 2.7. In all of the nine cases, the solutions behave exactly the way predicted by the bifurcation diagram and the computed plateau values are in good agreement with the analytical ones.

2.4.5 2-D Examples

In this section, we test the performance of the proposed fast explicit operator splitting method on two 2-D examples. Our goal is to clearly demonstrate the difference in the solutions of the BL and MBL equations. To achieve high resolution, we use the fifth-order WENO5 reconstruction.

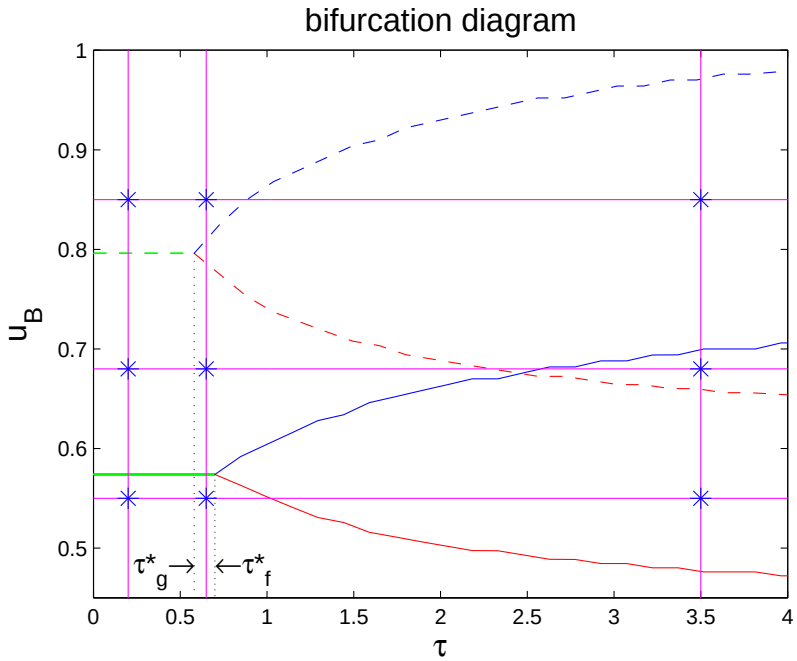

Figure 2.6: The zoom-in view of the bifurcation diagram given in Figure 2.1 along with the parameter values (marked by "×" signs) chosen in the nine experiments reported in Figure 2.7.

Example 4: Rotational BL and MBL Equations

We first consider the 2-D rotational BL,

$$u_t + \nabla \cdot (\boldsymbol{V} f(u)) = 0, \tag{2.34}$$

and MBL equations:

$$u_t + \nabla \cdot (\boldsymbol{V} f(u)) = \varepsilon \Delta u + \varepsilon^2 \tau \Delta u_t, \tag{2.35}$$

where f is given by (2.2), $M = 2$, $\tau = 5$ and $\boldsymbol{V}(x, z) = (z, -x)^T$. We select the computational domain to be $[-2, 2] \times [-2, 2]$ and prescribe the following initial condition:

$$u(x, z, 0) = \begin{cases} \sqrt{\dfrac{2}{3}}, & \text{if } x^2 + z^2 \leq 1,\ x > 0,\ z > 0, \\ 0, & \text{otherwise.} \end{cases}$$

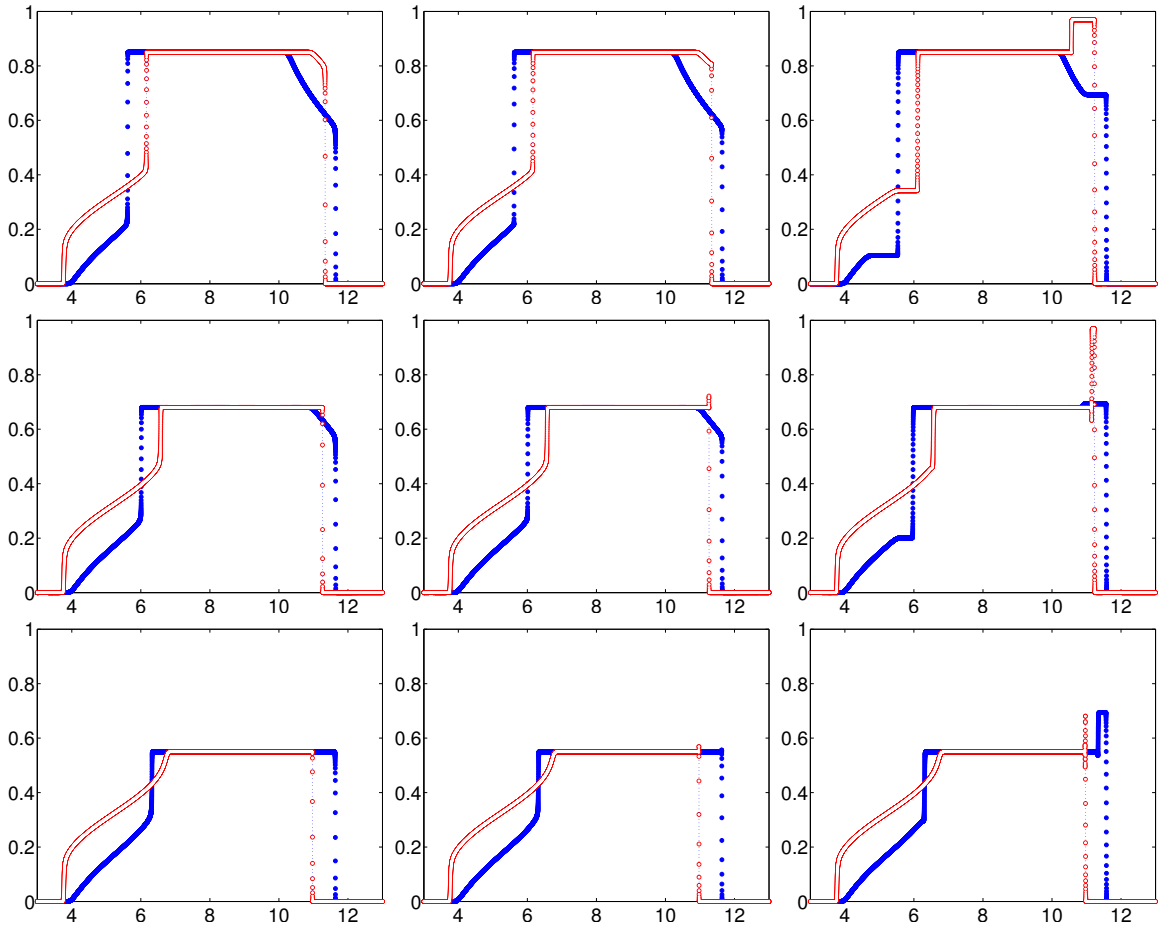

Figure 2.7: Solutions of the MBL equation (2.5) with the f flux (2.2) (filled circles) and g flux (2.3) (empty circles) computed at time $T = 1.2$ using $N = 16384$. For each of the nine plots, the initial data (2.33) corresponds to the nine (τ, u_B) pairs given in Table 2.7 and also marked in Figure 2.6.

The solutions of the BL equation (2.34) and MBL equation (2.35) computed at time $T = 1.5$ using a uniform 512×512 grid are shown in Figures 2.8 and 2.9, respectively. As one can see, the solution of the MBL equation develops a plateau at the rotational shock front, as one can expect based on the traveling wave analysis described in Section 2.2.3.

Example 5: Two-Dimensional BL and MBL Equations with Gravitation

In the final example, we solve the following 2-D BL equation (2.19) and the MBL equation (2.18) with the fluxes $F(u) = f(u)$ and $G(u) = g(u)$ given by (2.2) and (2.3), respectively, with $M = 1/2$, $C = 2$ and $\tau = 2.5$. We study two different initial

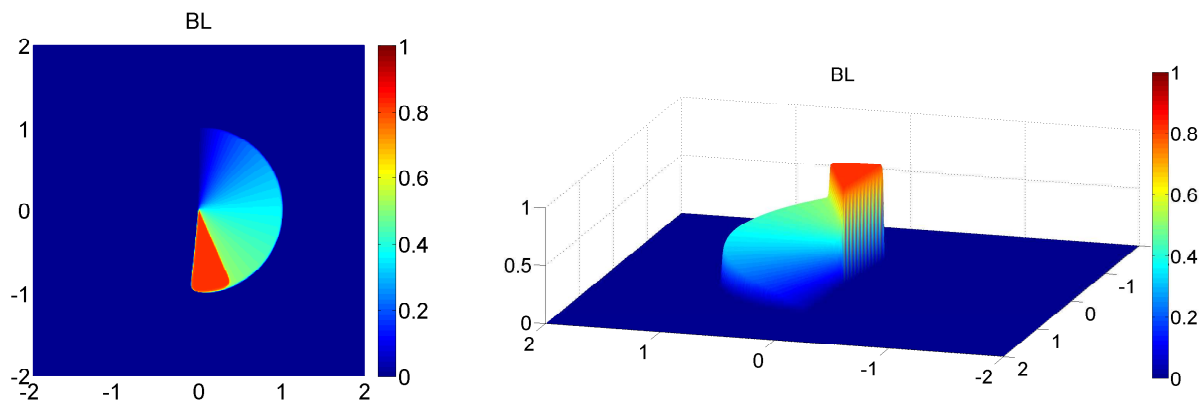

Figure 2.8: Example 4: Solution of the BL equation: top (left) and 3-D (right) views.

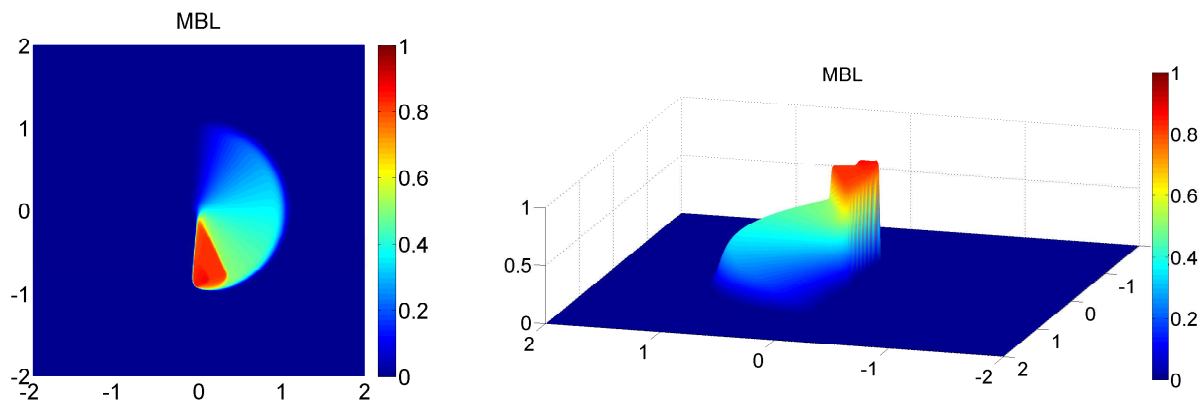

Figure 2.9: Example 4: Solution of the MBL equation: top (left) and 3-D (right) views.

conditions: a smooth 2-D Gaussian cut off by a plateau at the level $u = 0.85$,

$$u(x, z, 0) = 5e^{-20(x^2+z^2)}, \tag{2.36}$$

considered on the square computational domain $[-1.25, 1.25] \times [-1.25, 1.25]$, and a nonsmooth

$$u(x, z, 0) = \begin{cases} 0.85, & \text{if } 0.75 \le |x| \le 2.25, \quad 0.75 \le |z| \le 2.25, \\ 0, & \text{otherwise}, \end{cases} \tag{2.37}$$

considered on the square computational domain $[0, 3] \times [0, 3]$. Both solutions are computed on a uniform 1024×1024 grid at time $T = 0.48$.

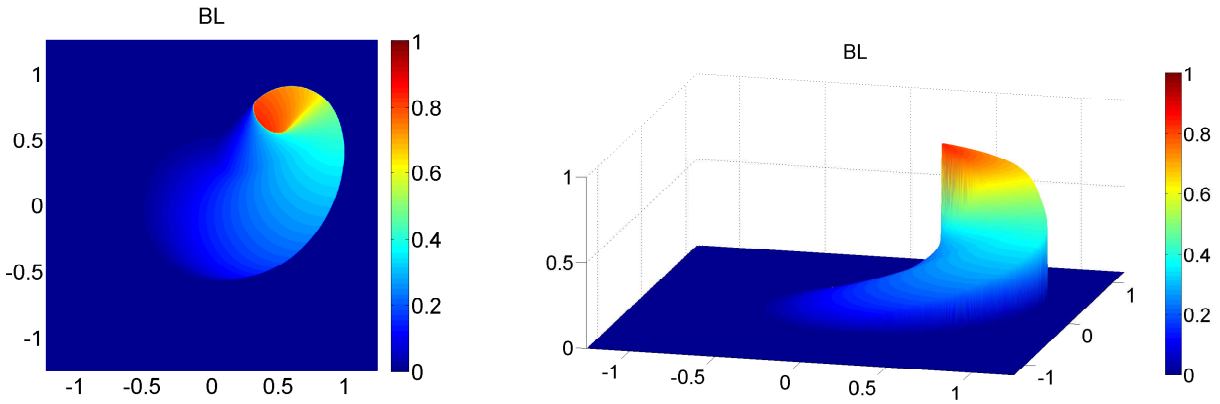

Figure 2.10: Example 5, initial condition (2.36): Solution of the BL equation: top (left) and 3-D (right) views.

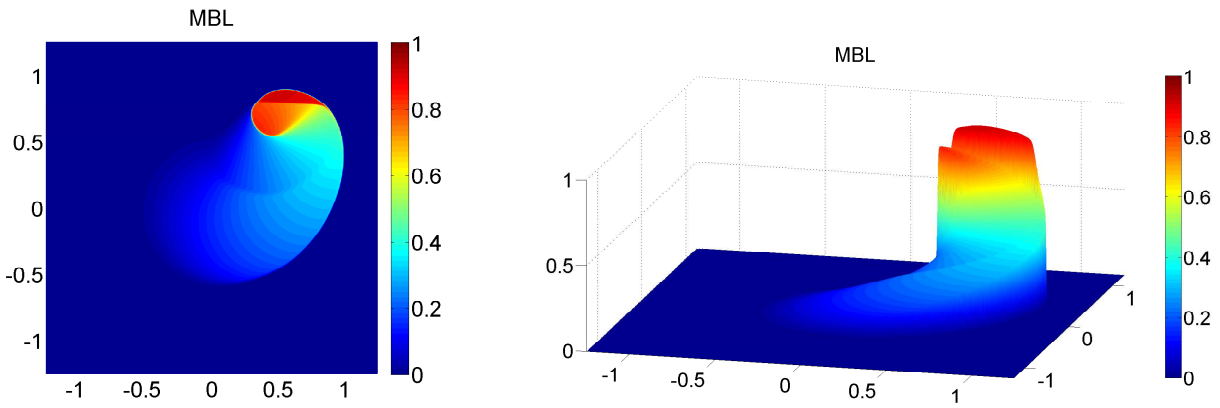

Figure 2.11: Example 5, initial condition (2.36): Solution of the MBL equation: top (left) and 3-D (right) views.

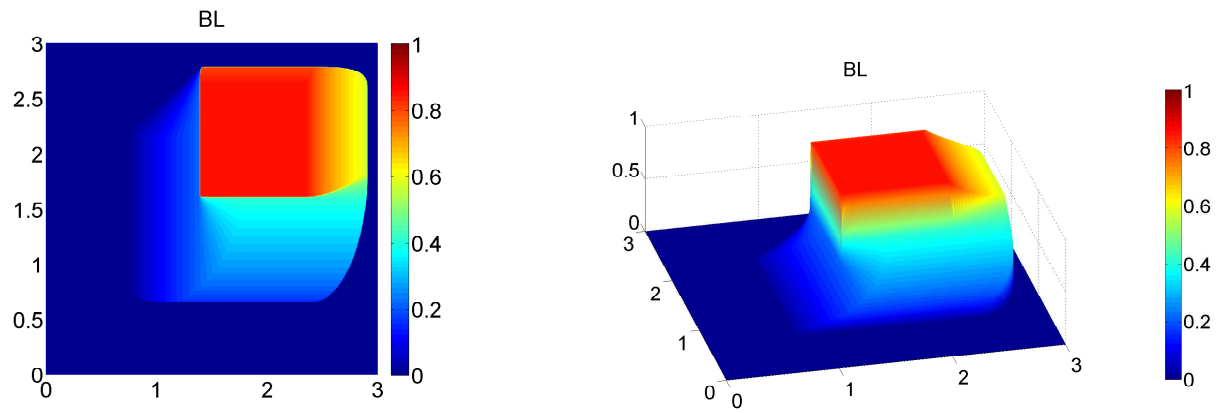

Figure 2.12: Example 5, initial condition (2.37): Solution of the BL equation: top (left) and 3-D (right) views.

Figures 2.10 and 2.11 show the results for the IVPs (2.19), (2.2), (2.3), (2.36) and (2.18), (2.2), (2.3), (2.36), respectively. Again, as one can expect, the solution

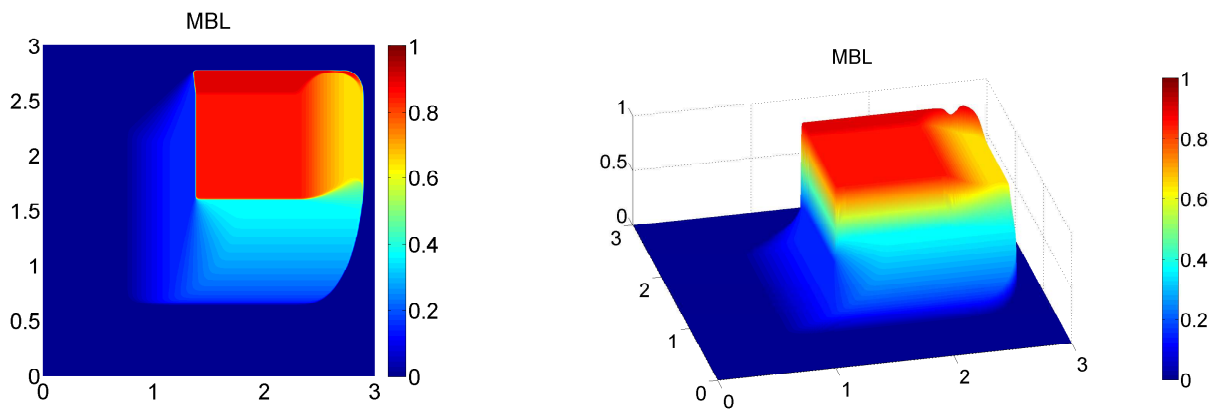

Figure 2.13: Example 5, initial condition (2.37): Solution of the MBL equation: top (left) and 3-D (right) views.

of the MBL equation (2.18) generates a clear plateau across the shock front in the z-direction, which is consistent with the traveling wave study presented in Section 2.2.3, according to which the parameter pair $(\tau, u_B) = (2.5, 0.85)$ falls into Case (i) for the flux f and into Case (ii) for the flux g.

Finally, if we use the initial condition (2.37), the results obtained for the BL equation (2.19), (2.2), (2.3) and MBL equation (2.18), (2.2), (2.3) are shown in Figures 2.12 and 2.13, respectively. Similarly to the previous case of the initial condition (2.36), the new plateau can be found near the shock front in the z-direction. However, because of the rarefaction wave created by the flux f in the x-direction, this plateau gets deformed at its upper-right corner.

Chapter 3

Fast and Stable Explicit Operator Splitting Methods for Phase-Field Models

Numerical simulations of phase-field models require long time computations and therefore it is necessary to develop efficient and highly accurate numerical methods. In this chapter, we propose fast and stable explicit operator splitting methods for both one- and two-dimensional nonlinear diffusion equations for thin film epitaxy with slope selection and the Cahn-Hilliard equation. The equations are split into nonlinear and linear parts. The nonlinear part is solved using a method of lines together with an efficient large stability domain explicit ODE solver. The linear part is solved by a pseudo-spectral method, which is based on the exact solution and thus has no stability restriction on the time-step size. We demonstrate the performance of the proposed methods on a number of one- and two-dimensional numerical examples, where different stages of coarsening such as the initial preparation, alternating rapid structural transition and slow motion can be clearly observed.

3.1 Introduction

Phase-field models have been recently introduced to describe interfacial phenomena. They were originally derived for the microstructure evolution and phase transition, but have been recently extended to many other physical phenomena, such as solid-solid transitions, growth of cancerous tumors, phase separation of block copolymers, dewetting and rupture of thin liquid films and infiltration of water into porous medium.

Two of these phase-field models have attracted much attention: the molecular beam epitaxy (MBE) equation with slope selection

$$u_t = -\delta\Delta^2 u + \nabla \cdot f(\nabla u), \quad (x, y) \in \Omega \subset \mathbb{R}^2,\ t \in (0, T], \tag{3.1}$$

and the Cahn-Hilliard (CH) equation

$$u_t = -\delta\Delta^2 u + \Delta f(u), \quad (x, y) \in \Omega \subset \mathbb{R}^2,\ t \in (0, T]. \tag{3.2}$$

In this chapter, we consider

$$f(\varphi) = \varphi|\varphi|^2 - \varphi,$$

for which the two phase-field models (3.1) and (3.2) become

$$u_t = -\delta\Delta^2 u + \nabla \cdot (|\nabla u|^2 \nabla u - \nabla u), \quad (x, y) \in \Omega \subset \mathbb{R}^2,\ t \in (0, T], \tag{3.3}$$

and

$$u_t = -\delta\Delta^2 u + \Delta(u^3 - u), \quad (x, y) \in \Omega \subset \mathbb{R}^2,\ t \in (0, T]. \tag{3.4}$$

In (3.3), u is a scaled height function of epitaxial growth of thin films in a co-moving frame and the parameter δ is a positive surface diffusion constant. In (3.4), u represents the concentration of one of the two metallic components of the

alloy, and the positive parameter δ represents the interfacial width, which is small compared to the characteristic length of the laboratory scale. An important feature of these two equations is that they can be viewed as the gradient flow of the following energy functionals:

$$E(u) = \int_{\Omega} \left[\frac{\delta}{2} |\Delta u|^2 + \frac{1}{4} (|\nabla u|^2 - 1)^2 \right] dxdy \tag{3.5}$$

for the MBE equation and

$$E(u) = \int_{\Omega} \left[\frac{\delta}{2} |\nabla u|^2 + \frac{1}{4} (u^2 - 1)^2 \right] dxdy \tag{3.6}$$

for the CH one. As it has been shown in [42, 43], both energy functionals decay in time:

$$E(u(t)) \leq E(u(s)), \ \forall t \geq s.$$

Development of highly accurate and efficient numerical methods for (3.3) and (3.4) is a challenging task. Since explicit schemes usually suffer from severe stability restrictions caused by the presence of high-order derivative terms and do not obey the energy decay property, semi-implicit schemes are widely used. In [65], a combined spectral and large time-stepping method was studied for the MBE equation, in which an extra term was added to substantially improve the stability condition. The same method was applied to the CH equation in [66]. However, this artificial stabilization term depends on the unknown numerical solutions and if it is taken improperly, the resulting numerical scheme would be unstable. In [67], unconditionally energy stable finite-difference schemes were introduced and an adaptive time-stepping strategy was proposed to select time-steps adaptively based on the time variation of the energy. This technique was also successfully applied in the simulations of the CH equation in [68]. In [69], a high-order and energy stable

scheme was developed to simulate some phase-field models by combining the semi-implicit spectral deferred correction method and the energy stable convex splitting technique. In [70], a set of unconditionally stable, unconditionally uniquely solvable and second-order schemes for general gradient flows of Ehrlich-Schwoebel energy type with a specific application to the MBE equation was presented. In addition, a variety of finite-element based unconditionally energy-stable schemes for the CH equation were proposed in [71, 72], including first- and second-order in time linear schemes as well as an adaptive time-stepping algorithm. A detailed review of the recent updates on numerical methods for the CH equation and its applicability to related energy-based models, including phase-field models, can be found in [73].

In this chapter, we develop accurate, efficient and robust explicit methods for both (3.3) and (3.4) subject to periodic boundary conditions. Our methods, which are described in detail in Section 3.2 and Section 3.3, are based on the large stability domain explicit Runge-Kutta methods [35, 37, 74, 75] and the fast explicit operator splitting method proposed in [18–21] (see also [22]) in the context of convection-diffusion equations.

Following the approach in [18–21], we split equation (3.3) into the nonlinear,

$$u_t = \nabla \cdot (|\nabla u|^2 \nabla u), \tag{3.7}$$

and linear,

$$u_t = -\Delta u - \delta \Delta^2 u, \tag{3.8}$$

parts. We denote by $\mathcal{S}_{\mathcal{N}}$ the *exact* solution operator associated with (3.7) and by $\mathcal{S}_{\mathcal{L}}$ the *exact* solution operator associated with (3.8). Notice that the corresponding energy functionals,

$$E_{\mathcal{N}}(u) = \frac{1}{4} \int_{\Omega} |\nabla u|^4 \, dxdy \tag{3.9}$$

and

$$E_{\mathcal{L}}(u) = \int_{\Omega} \left(\frac{\delta}{2}|\Delta u|^2 - \frac{1}{2}|\nabla u|^2 + \frac{1}{4} \right) dxdy \tag{3.10}$$

decay. Then, introducing a (small) splitting step Δt, the solution of the original equation (3.3) (which is assumed to be available at time t) is evolved using the Strang splitting method [5–7], one step of which can be written as

$$u(x, y, t + \Delta t) = \mathcal{S}_{\mathcal{L}}(\Delta t/2)\mathcal{S}_{\mathcal{N}}(\Delta t)\mathcal{S}_{\mathcal{L}}(\Delta t/2)u(x, y, t).$$

A similar splitting approach is applied to equation (3.4), for which the linear part is still (3.8) and the nonlinear one is

$$u_t = \Delta(u^3). \tag{3.11}$$

As in the case of the MBE equation, the corresponding energy functionals,

$$E_{\mathcal{N}}(u) = \frac{1}{4} \int_{\Omega} u^4 \, dxdy \tag{3.12}$$

and

$$E_{\mathcal{L}}(u) = \int_{\Omega} \left(\frac{\delta}{2}|\nabla u|^2 - \frac{1}{2}u^2 + \frac{1}{4} \right) dxdy \tag{3.13}$$

decay. We stress that even though the linear parts of equations (3.3) and (3.4) are the same, the functionals (3.10) and (3.13) are different since they are associated with the corresponding parts of the energy functionals (3.5) and (3.6).

In order to implement the splitting method, the exact solution operators $\mathcal{S}_{\mathcal{N}}$ and $\mathcal{S}_{\mathcal{L}}$ have to be replaced by their numerical approximations. Note that one of the main advantages of the operator splitting technique is the fact that the nonlinear, (3.7) and (3.11), and linear, (3.8), subproblems, which are of different nature, can be solved numerically by different methods. First, using the method of lines, (3.7)

and (3.11) can be reduced to systems of ODEs, which can be efficiently and accurately integrated by large stability domain explicit ODE solvers [35, 37, 74, 75]. Second, since (3.8) is linear, one can solve it (practically) exactly using, for example, the pseudo-spectral method. This way, no stability restrictions on solving (3.8) are imposed. A detailed description of an efficient implementation of the proposed fast and stable explicit operator splitting methods is given in Section 3.2 and Section 3.3.

The chapter is organized as follows. In Section 3.2, we build $2m$th-order semi-discrete finite-difference schemes for (3.7) and (3.11). The resulting stiff system of ODE is then solved by an efficient large stability domain explicit ODE solver [76, 77]. In Section 3.3, we develop a pseudo-spectral method for the linear equation (3.8). In Section 3.5, we demonstrate the performance of the proposed fast and stable explicit operator splitting methods on a number of 1-D and 2-D numerical examples, where different stages of coarsening such as the initial preparation, alternating rapid structural transition and slow motion can be clearly observed.

3.2 Finite-Difference Methods for (3.7) and (3.11)

In this section, we propose efficient explicit finite-difference methods for the degenerate parabolic equations (3.7) and (3.11). These methods are based on the semi-discretization of (3.7) and (3.11) followed by the use of an efficient and accurate ODE solver. The ODE solver will be utilized to evolve the solutions of (3.7) and (3.11) from time t to $t + \Delta t$. We note that in a general case the time-steps of the ODE solver denoted by Δt_{ODE} will be smaller than the splitting step Δt so that the approximation of $\mathcal{S}_{\mathcal{N}}(\Delta t)$ will typically require several Δt_{ODE} steps.

3.2.1 Finite-Difference Schemes for $u_t = (u_x^3)_x$

In this section, we design $2m$th-order centered-difference schemes for the 1-D version of (3.7):

$$u_t = (u_x^3)_x, \quad x \in [0, L],\ t \in (0, T]. \tag{3.14}$$

We consider a uniform grid with nodes x_j, such that $x_{j+1} - x_j = \Delta x, \forall j$, and introduce the following $2m$th-order discrete approximation of the $\frac{\partial}{\partial x}$ operator:

$$(\psi_x)_j := \sum_{p=-m}^{m} \alpha_p \psi_{j+p} = \psi_x(x_j) + \mathcal{O}((\Delta x)^{2m}). \tag{3.15}$$

For example, when $m = 2$, we obtain a fourth-order centered-difference approximation by taking

$$\alpha_1 = -\alpha_{-1} = \frac{2}{3\Delta x}, \quad \alpha_2 = -\alpha_{-2} = -\frac{1}{12\Delta x}.$$

Equipped with the above approximation of spacial derivatives, we discretize equation (3.14) using the method of lines as follows:

$$\frac{du_j}{dt}(t) = \sum_{p=-m}^{m} \alpha_p H_{j+p}(t) =: F_j(t), \tag{3.16}$$

where $u_j(t)$ denotes the computed point value of the solution at (x_j, t), and

$$H_j(t) := (u_x)_j^3(t) \quad \text{with} \quad (u_x)_j(t) := \sum_{p=-m}^{m} \alpha_p u_{j+p}(t). \tag{3.17}$$

Note that the above quantities depend on t, but for the sake of brevity we will suppress this dependence from now on.

Remark 3.2.1 One can show that the coefficients $\{\alpha_p\}$ satisfy the following

conditions:

$$\alpha_0 = 0 \quad \text{and} \quad \alpha_p + \alpha_{-p} = 0,\ p \neq 0. \tag{3.18}$$

Theorem 3.2.1 *The semi-discrete schemes (3.16), (3.17) satisfy the following energy decay property:*

$$\frac{d}{dt} E_{\mathcal{N}}^{\Delta} \leq 0,$$

where $E_{\mathcal{N}}^{\Delta}$ is a 1-D discrete version of the energy functional (3.9):

$$E_{\mathcal{N}}^{\Delta} := \frac{1}{4} \sum_j (u_x)_j^4 \Delta x.$$

Proof: Using (3.16)–(3.18) and the periodicity of computed solutions, one can obtain the following energy estimate:

$$\begin{aligned}
\frac{d}{dt}\left(\frac{1}{4}\sum_j (u_x)_j^4\right) &= \sum_j (u_x)_j^3 \frac{d}{dt}[(u_x)_j] \overset{(3.17)}{=} \sum_j H_j \frac{d}{dt}\left[\sum_{p=-m}^{m} \alpha_p u_{j+p}\right] \\
&\overset{(3.16)}{=} \sum_j H_j \sum_{p=-m}^{m} \alpha_p F_{j+p} = \sum_{p=-m}^{m} \alpha_p \sum_j H_j F_{j+p} = \sum_{p=-m}^{m} \alpha_p \sum_j H_{j-p} F_j \\
&= \sum_j F_j \sum_{p=-m}^{m} \alpha_p H_{j-p} = \sum_j F_j \sum_{p=-m}^{m} \alpha_{-p} H_{j+p} \\
&\overset{(3.18)}{=} \sum_j F_j \sum_{p=-m}^{m} (-\alpha_p) H_{j+p} \overset{(3.16)}{=} -\sum_j F_j^2 \leq 0.
\end{aligned}$$

■

3.2.2 Finite-Difference Schemes for $u_t = \nabla \cdot [|\nabla u|^2 \nabla u]$

We now turn to the 2-D equation (3.7). We consider a uniform grid with nodes (x_j, y_k), such that $x_{j+1} - x_j = \Delta x, \forall j,\ y_{k+1} - y_k = \Delta y, \forall k$, and introduce the

following $2m$th-order discrete approximation of the $\frac{\partial}{\partial x}$ and $\frac{\partial}{\partial y}$ operators:

$$
\begin{aligned}
(\psi_x)_{j,k} &:= \sum_{p=-m}^{m} \alpha_p \psi_{j+p,k} = \psi_x(x_j, y_k) + \mathcal{O}((\Delta x)^{2m}), \\
(\psi_y)_{j,k} &:= \sum_{p=-m}^{m} \beta_p \psi_{j,k+p} = \psi_y(x_j, y_k) + \mathcal{O}((\Delta y)^{2m}).
\end{aligned}
\tag{3.19}
$$

For example, when $m = 2$, we obtain a fourth-order centered-difference approximation by taking

$$
\alpha_1 = -\alpha_{-1} = \frac{2}{3\Delta x}, \quad \alpha_2 = -\alpha_{-2} = -\frac{1}{12\Delta x},
$$

$$
\beta_1 = -\beta_{-1} = \frac{2}{3\Delta y}, \quad \beta_2 = -\beta_{-2} = -\frac{1}{12\Delta y}.
$$

Equipped with the above approximation of spacial derivatives, $2m$th-order semi-discrete finite-difference schemes for (3.7) read:

$$
\frac{du_{j,k}}{dt} = \sum_{p=-m}^{m} \alpha_p H^x_{j+p,k} + \sum_{p=-m}^{m} \beta_p H^y_{j,k+p} =: F_{j,k}, \tag{3.20}
$$

where

$$
H^x_{j,k} := (u_x)^3_{j,k} + (u_y)^2_{j,k}(u_x)_{j,k} \quad \text{and} \quad H^y_{j,k} := (u_y)^3_{j,k} + (u_x)^2_{j,k}(u_y)_{j,k} \tag{3.21}
$$

with

$$
(u_x)_{j,k} := \sum_{p=-m}^{m} \alpha_p u_{j+p,k} \quad \text{and} \quad (u_y)_{j,k} := \sum_{p=-m}^{m} \beta_p u_{j,k+p}. \tag{3.22}
$$

Remark 3.2.2 One can show that the coefficients $\{\alpha_p\}$ and $\{\beta_p\}$ satisfy the following conditions:

$$
\alpha_0 = 0, \quad \beta_0 = 0 \quad \text{and} \quad \alpha_p + \alpha_{-p} = 0, \quad \beta_p + \beta_{-p} = 0, \quad p \neq 0. \tag{3.23}
$$

Theorem 3.2.2 *The semi-discrete schemes (3.20)–(3.22) satisfy the following energy decay property:*

$$\frac{d}{dt}E_{\mathcal{N}}^{\Delta} \leq 0,$$

where $E_{\mathcal{N}}^{\Delta}$ is a 2-D discrete version of the energy functional (3.9):

$$E_{\mathcal{N}}^{\Delta} := \frac{1}{4}\sum_{j} |\nabla_h u_{j,k}|^4 \Delta x \Delta y$$

with $\nabla_h u_{j,k} := ((u_x)_{j,k}, (u_y)_{j,k})^T$.

Proof: Using (3.20)–(3.23) and the periodicity of computed solutions, one can obtain the following energy estimate:

$$\begin{aligned}
\frac{d}{dt}\left(\frac{1}{4}\sum_{j,k}|\nabla_h u_{j,k}|^4\right) &\overset{(3.21)}{=} \sum_{j,k} H^x_{j,k}\frac{d}{dt}[(u_x)_{j,k}] + \sum_{j,k} H^y_{j,k}\frac{d}{dt}[(u_y)_{j,k}] \\
&\overset{(3.22)}{=} \sum_{j,k} H^x_{j,k}\frac{d}{dt}\left[\sum_{p=-m}^{m}\alpha_p u_{j+p,k}\right] + \sum_{j,k} H^y_{j,k}\frac{d}{dt}\left[\sum_{p=-m}^{m}\beta_p u_{j,k+p}\right] \\
&\overset{(3.20)}{=} \sum_{j,k} H^x_{j,k}\sum_{p=-m}^{m}\alpha_p F_{j+p,k} + \sum_{j,k} H^y_{j,k}\sum_{p=-m}^{m}\beta_p F_{j,k+p} \\
&\overset{(3.23)}{=} -\sum_{j,k} F_{j,k}\sum_{p=-m}^{m}\alpha_p H^x_{j+p,k} - \sum_{j,k} F_{j,k}\sum_{p=-m}^{m}\beta_p H^y_{j,k+p} \\
&\overset{(3.20)}{=} -\sum_{j,k} F^2_{j,k} \leq 0.
\end{aligned}$$

■

3.2.3 Finite-Difference Schemes for $u_t = \Delta(u^3)$

We now design semi-discrete finite-difference schemes for the 2-D CH equation (3.11). We use the same grids and the same $2m$th-order discrete approximation of the $\frac{\partial}{\partial x}$ and $\frac{\partial}{\partial y}$ operators as in Section 3.2.2. Then, $2m$th-order semi-discrete

finite-difference schemes for (3.11) read:

$$\frac{du_{j,k}}{dt} = \sum_{p=-m}^{m} \alpha_p H^x_{j+p,k} + \sum_{p=-m}^{m} \beta_p H^y_{j,k+p} =: F_{j,k}, \tag{3.24}$$

where

$$H^x_{j,k} := \sum_{p=-m}^{m} \alpha_p u^3_{j+p,k} \quad \text{and} \quad H^y_{j,k} := \sum_{p=-m}^{m} \beta_p u^3_{j,k+p}. \tag{3.25}$$

Theorem 3.2.3 *The semi-discrete schemes (3.24), (3.25) satisfy the following energy decay property:*

$$\frac{d}{dt} E^{\Delta}_{\mathcal{N}} \leq 0,$$

where $E^{\Delta}_{\mathcal{N}}$ is a 2-D discrete version of the energy functional (3.12):

$$E^{\Delta}_{\mathcal{N}} := \frac{1}{4} \sum_{j} u^4_{j,k} \Delta x \Delta y.$$

Proof: Using (3.23)–(3.25) and the periodicity of computed solutions, one can obtain the following energy estimate:

$$\begin{aligned}
\frac{d}{dt}\left(\frac{1}{4}\sum_{j,k} u^4_{j,k}\right) &= \sum_{j,k} u^3_{j,k} \frac{du_{j,k}}{dt} \overset{(3.24)}{=} \sum_{j,k} \sum_{p=-m}^{m} \alpha_p H^x_{j+p,k} u^3_{j,k} + \sum_{j,k} \sum_{p=-m}^{m} \beta_p H^y_{j,k+p} u^3_{j,k} \\
&\overset{(3.23)}{=} -\sum_{j,k} H^x_{j,k} \sum_{p=-m}^{m} \alpha_p u^3_{j+p,k} - \sum_{j,k} H^y_{j,k+p} \sum_{p=-m}^{m} \beta_p u^3_{j,k+p} \\
&\overset{(3.25)}{=} -\sum_{j,k} \left[(H^x_{j,k})^2 + (H^y_{j,k})^2\right] \leq 0.
\end{aligned}$$

■

3.2.4 Large Stability Domain Explicit ODE Solver

The ODE systems (3.16), (3.20) and (3.24) have to be solved numerically. Recall that explicit ODE solvers typically require time-steps to be $\Delta t_{\text{ODE}} \sim (\Delta x)^2$, while implicit ODE solvers can be made unconditionally stable. However, the accuracy requirements would limit time-step size and since a large nonlinear algebraic system of equations has to be solved at each time-step, implicit methods may not be efficient. Here, we apply the explicit third-order large stability domain Runge-Kutta method, developed in [37, 77]. This method belongs to a class of Runge-Kutta-Chebyshev methods (see, e.g., [75, 78–81]), which allow one to use much larger time-steps compared with the standard explicit Runge-Kutta methods. In practice, when the problem is not too stiff as in the case of ODEs arising in finite-difference approximation of parabolic PDEs, these methods preserve all the advantages of explicit methods and are typically more efficient than implicit methods (see [35, 37, 74, 78, 81] for details). We have implemented the code DUMKA3 [77], which incorporates the embedded formulas that permit an efficient stepsize control. The efficiency of DUMKA3 is further improved when the user provides an upper bound on the time-step stability restriction for the forward Euler method. We therefore establish such bounds in the following three theorems.

Theorem 3.2.4 *Assume that the system of ODEs (3.16), (3.17) is numerically integrated by the forward Euler method from time t to $t + \Delta t_{\text{FE}}$ and that the following CFL condition holds:*

$$\Delta t_{\text{FE}} \leq \frac{1}{am} \cdot \frac{1}{\max\limits_j (u_x)_j^2}, \quad a := \sum_{p=-m}^{m} \alpha_p^2, \tag{3.26}$$

where α_p are the coefficients in (3.15) and $(u_x)_j$ are given by (3.17). Then

$$\|u(t + \Delta t_{\text{FE}})\|_{L^2} \leq \|u(t)\|_{L^2}, \tag{3.27}$$

where $\|u(t)\|_{L^2} := \sqrt{\sum_j u_j^2(t)\Delta x}$.

Theorem 3.2.5 *Assume that the system of ODEs (3.20)–(3.22) is numerically integrated by the forward Euler method from time* t *to* $t + \Delta t_{\mathrm{FE}}$ *and that the following CFL condition holds:*

$$\Delta t_{\mathrm{FE}} \leq \frac{1}{4m \cdot \max(a,b)} \cdot \frac{1}{\max\limits_{j,k}\{(u_x)_{j,k}^2, (u_y)_{j,k}^2\}}, \quad a := \sum_{p=-m}^{m} \alpha_p^2, \; b := \sum_{p=-m}^{m} \beta_p^2, \tag{3.28}$$

where α_p *and* β_p *are the coefficients in (3.19) and* $(u_x)_{j,k}$ *and* $(u_y)_{j,k}$ *are given by (3.22). Then*

$$\|u(t + \Delta t_{\mathrm{FE}})\|_{L^2} \leq \|u(t)\|_{L^2}, \tag{3.29}$$

where $\|u(t)\|_{L^2} := \sqrt{\sum_{j,k} u_{j,k}^2(t)\Delta x \Delta y}$.

Theorem 3.2.6 *Assume that the system of ODEs (3.24), (3.25) is numerically integrated by the forward Euler method from time* t *to* $t + \Delta t_{\mathrm{FE}}$ *and that the following CFL condition holds:*

$$\Delta t_{\mathrm{FE}} \leq \frac{1}{6m \cdot \max(a,b)} \cdot \frac{1}{\max\limits_{j,k} u_{j,k}^2}. \tag{3.30}$$

Then,

$$\|u(t + \Delta t_{\mathrm{FE}})\|_{L^2} \leq \|u(t)\|_{L^2}, \tag{3.31}$$

with the same a *and* b *as in Theorem 3.2.5.*

Proofs of Theorem 3.2.4, Theorem 3.2.5 and Theorem 3.2.6 are provided in Appendix A.

Remark 3.2.3 We would like to emphasize that the code DUMKA3 automatically selects time-steps so that in average the selected time-steps Δt_{ODE} are much larger than Δt_{FE}.

3.3 Pseudo-Spectral Methods for (3.8)

In this section, we describe the (exact) pseudo-spectral solver for equation (3.8) and its 1-D version.

3.3.1 One-Dimensional Pseudo-Spectral Method

We consider the 1-D equation,

$$u_t = -u_{xx} - \delta u_{xxxx}, \quad x \in [0, L],\ t \in (0, T], \tag{3.32}$$

subject to the L-periodic boundary conditions.

We first use the FFT algorithm to compute the discrete Fourier coefficients $\{\widehat{u}_m(t)\}$ from the available point values $\{u_j(t)\}$. This gives us the following spectral approximation of u on $[0, L]$:

$$u(x, t) \approx \sum_m \widehat{u}_m(t) e^{i\frac{2\pi m x}{L}}. \tag{3.33}$$

We then substitute (3.33) into (3.32) and obtain very simple linear ODEs for the discrete Fourier coefficients of u,

$$\frac{d}{dt}\widehat{u}_m(t) = (s - \delta s^2)\widehat{u}_m(t), \quad s = \left(\frac{2\pi m}{L}\right)^2,$$

which can be solved exactly:

$$\widehat{u}_m(t + \Delta t) = e^{(s-\delta s^2)\Delta t}\ \widehat{u}_m(t).$$

Finally, we use the inverse FFT algorithm to obtain the point values of the solution at the new time level, $\{u_j(t + \Delta t)\}$, out of the set of the discrete Fourier coefficients $\{\widehat{u}_m(t + \Delta t)\}$.

3.3.2 Two-Dimensional Pseudo-Spectral Method

We now solve the 2-D equation (3.8),

$$u_t = -(u_{xx} + u_{yy}) - \delta(u_{xxxx} + 2u_{xxyy} + u_{yyyy}),$$

on a rectangular domain $\Omega = [0, L_x] \times [0, L_y]$ with the L_x- and L_y-periodic boundary conditions in the x- and y-directions, respectively.

Similar to the 1-D case, we apply the FFT algorithm and obtain very simple linear ODEs for the discrete Fourier coefficients of u,

$$\frac{d}{dt}\widehat{u}_{m,\ell}(t) = (s - \delta s^2)\widehat{u}_{m,\ell}(t), \quad s = \left(\frac{2\pi m}{L_x}\right)^2 + \left(\frac{2\pi \ell}{L_y}\right)^2. \tag{3.34}$$

The exact solution of (3.34) is

$$\widehat{u}_{m,\ell}(t + \Delta t) = e^{(s-\delta s^2)\Delta t}\ \widehat{u}_{m,\ell}(t).$$

Finally, we apply the inverse FFT algorithm to obtain the point values of the solution at the new time level, $\{u_{j,k}(t + \Delta t)\}$, out of the set of the discrete Fourier coefficients $\{\widehat{u}_{m,\ell}(t + \Delta t)\}$.

Remark 3.3.1 Using Parseval's theorem and the fact that $e^{(s-\delta s^2)\Delta t} \le e^{\frac{\Delta t}{4\delta}}$, we obtain the following result on stability of the pseudo-spectral methods:

$$\|u(t + \Delta t)\|_{L^2} \le e^{\frac{\Delta t}{4\delta}} \|u(t)\|_{L^2},$$

which is true in both the 1-D and 2-D cases.

3.4 Adaptive Splitting Time-Stepping Strategy

For practical applications, the efficiency of splitting methods hinges on its ability to use (relatively) large time-steps (see, e.g., [18–22]). Our numerical experiments indicate that taking $\Delta t = \delta/100$ for the MBE equations and $\Delta t = \delta/10$ for the CH equation leads to accurate results. However, one expects such a small Δt is only required when the phase transition occurs and the solution changes quite rapidly. At other times and especially the solution is close to its steady state, it might be safe to use much larger Δt. We therefore explore an adaptive splitting time-stepping strategy: We would like to use small Δt only whenever necessary.

To design an adaptive approach, we need to measure the solution variation. This can be done using either the energy or solution roughness at time t, which is defined by

$$w(t) = \sqrt{\frac{1}{|\Omega|} \int_{\Omega} [u(x,y,t) - \bar{u}(t)]^2 \, dxdy}, \tag{3.35}$$

where

$$\bar{u}(t) = \frac{1}{|\Omega|} \int_{\Omega} u(x,y,t) \, dxdy \tag{3.36}$$

is the mean height at time t.

We adjust the size of splitting steps using the following roughness-dependent monitor function introduced in [67]

$$\Delta t = \max\left(\Delta t_{\min}, \ \frac{\Delta t_{\max}}{\sqrt{1 + \alpha |w'(t)|^2}}\right), \quad \alpha = \text{Const.} \tag{3.37}$$

Here, $\Delta t_{\min}$ is the smallest splitting step, which is taken to be either $\Delta t_{\min} = \delta/100$ (for the MBE equations) or $\Delta t_{\min} = \delta/10$ (for the CH equation), $\Delta t_{\max}$ is the largest allowed splitting step, and α is a positive adaption constant.

Notice that large $|w'(t)|$ will lead to small splitting step, which corresponds to

Example	Number of grid points	Final time	Splitting step	CPU time
1	256	240	constant	3.2805
			adaptive	0.9659
2	256×256	30	constant	4601.9
			adaptive	838.9
3	512×512	80000	constant	223370
			adaptive	38775
4	128×128	20	constant	504.09
			adaptive	125.86

Table 3.1: CPU times for Examples 1–4 in Section 3.5.

the case of rapid change of roughness or quick motion of the structural transition from one stage to the next one. Similarly, small $|w'(t)|$ yields large splitting step, which corresponds to the slow MBE growth or slow phase interface motion.

Remark 3.4.1 A similar adaptive strategy can be designed by replacing $w(t)$ with $E(t)$. However, our numerical experiments indicate the roughness-based strategy is more robust than the energy-based one.

Our numerical experiments reported in Section 3.5 suggest that the adaptive splitting time-stepping strategy can lead to a substantial reduction of the CPU time without significantly affecting the accuracy of the computed solution. The data on the CPU time reduction achieved in different numerical examples are presented in Table 3.1: In average, the adaptive method is about 3–6 times more efficient.

3.5 Numerical Examples

In this section, we illustrate the performance of our fast and stable explicit operator splitting methods on several 1-D and 2-D examples. When solving equation (3.7) and (3.11), we use the fourth-order finite-difference schemes developed in Section 2 (in Example 5, we also use the sixth-order scheme). Both constant and adaptive

splitting steps are employed to obtain numerical solutions. The adaptive splitting step is determined by (3.37) with the values $\Delta t_{\min}$, $\Delta t_{\max}$ and α being specified in each example.

To verify the rates of convergence of the proposed methods, we measure the difference between the solutions computed at the same time level on two consecutive grids using the L^1- and L^∞-errors, which are defined as follows:

$$||u^{N,\Delta t_1} - u^{N/2,\Delta t_2}||_1 := \frac{L_x L_y}{N^2} \sum_{j=1}^{N} \sum_{k=1}^{N} |u_{j,k}^{N,\Delta t_1} - u_{j,k}^{N/2,\Delta t_2}|,$$

and

$$||u^{N,\Delta t_1} - u^{N/2,\Delta t_2}||_\infty := \max_{1 \le j,k \le N} |u_{j,k}^{N,\Delta t_1} - u_{j,k}^{N/2,\Delta t_2}|,$$

where $u^{N,\Delta t} := \{u_{j,k}^N\}$ is a numerical solution obtained with a uniform $N \times N$ grid and a constant splitting step Δt at some time level. Then, to measure the experimental convergence rates, we use the ratio of errors:

$$r = \log_2 \left(\frac{||u^{N/2,\Delta t_2} - u^{N/4,\Delta t_3}||}{||u^{N,\Delta t_1} - u^{N/2,\Delta t_2}||} \right),$$

where we either take $\Delta t_1 = \Delta t,\ \Delta t_2 = 2\Delta t$ and $\Delta t_3 = 4\Delta t$ or fix the splitting step and set $\Delta t_1 = \Delta t_2 = \Delta t_3 = \Delta t$.

In the 1-D case, the rates are computed similarly.

Example 1: One-Dimensional Morphological Instability

We first consider the 1-D MBE equation

$$u_t = (u_x^3)_x - u_{xx} - u_{xxxx},$$

subject to the initial condition

$$u(x,0) = 0.1\Big(\sin\frac{\pi x}{2} + \sin\frac{2\pi x}{3} + \sin \pi x\Big), \quad x \in [0,12].$$

This example was studied in [43] to observe the morphological instability due to the nonlinear interaction.

We compute the solution until the final time $t = 240$ with a constant splitting step $\Delta t = 10^{-1}$ on the uniform grid with $N = 256$. Figure 3.1 shows a sequence of snapshots of the surface height at different times. As one can observe, the initial oscillation is damped by $t = 1$. After a relatively long period of "buffering" time, a new larger scale structure emerges, then it increases and finally the steady state is reached by $t = 240$.

Compared to the results reported in [43], our steady state is in a good agreement with the one obtained there, while the "buffering" time evolution is very different. We therefore reduce the splitting step by a factor of 10 and repeat the computation with $\Delta t = 10^{-2}$. The obtained solution, plotted in Figure 3.2 (solid line), now matches the results in [43]: The structure emerges earlier and the steady state is reached by $t = 60$.

The time evolution process can be monitored by plotting the energy (3.5) and roughness (3.35), see Figure 3.3. One can observe that initially both energy and roughness decay rapidly. However, after a relatively long period of time, roughness starts to grow, which is exactly the morphological instability in the rough-smooth-rough pattern. Notice that the flat tail in Figure 3.3(b) and (d) indicates that the steady state is reached much later when $\Delta t = 10^{-1}$ is used. To improve the efficiency of the proposed fast and stable explicit operator splitting methods, we implement the adaptive strategy described in Section 4. Here, we use $\Delta t_{\min} = 10^{-2}$, $\Delta t_{\max} = 10^{-1}$ and $\alpha = 10^{3}$. The obtained solution is shown in Figure

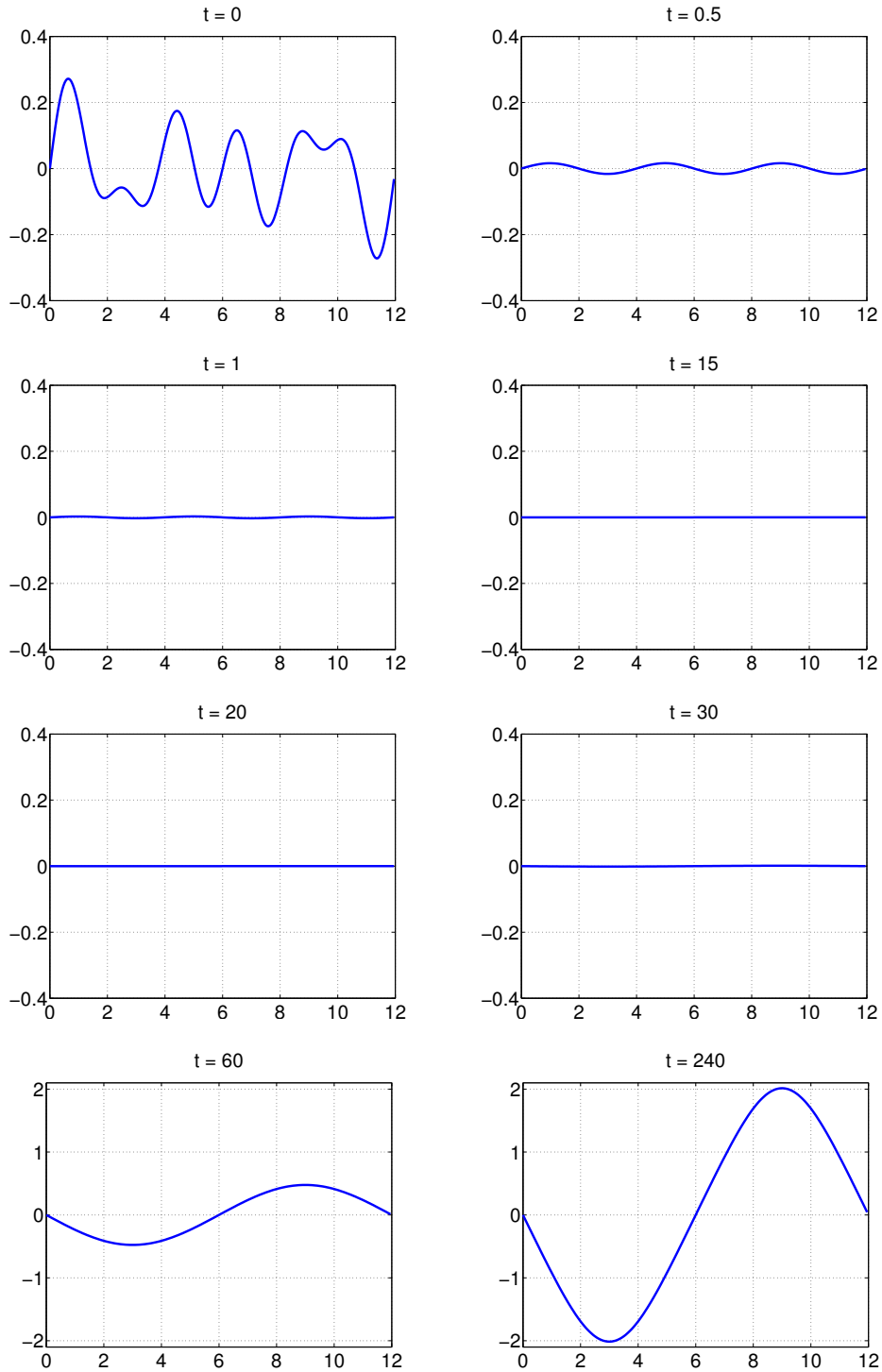

Figure 3.1: Example 1: u computed with $\Delta t = 10^{-1}$.

3.2 (dashed line), and the corresponding energy and roughness are plotted in Figure 3.3 (dashed line). As one can see, the adaptive solution practically coincides with the solution computed with $\Delta t = 10^{-2}$. It is instructive to check what splitting

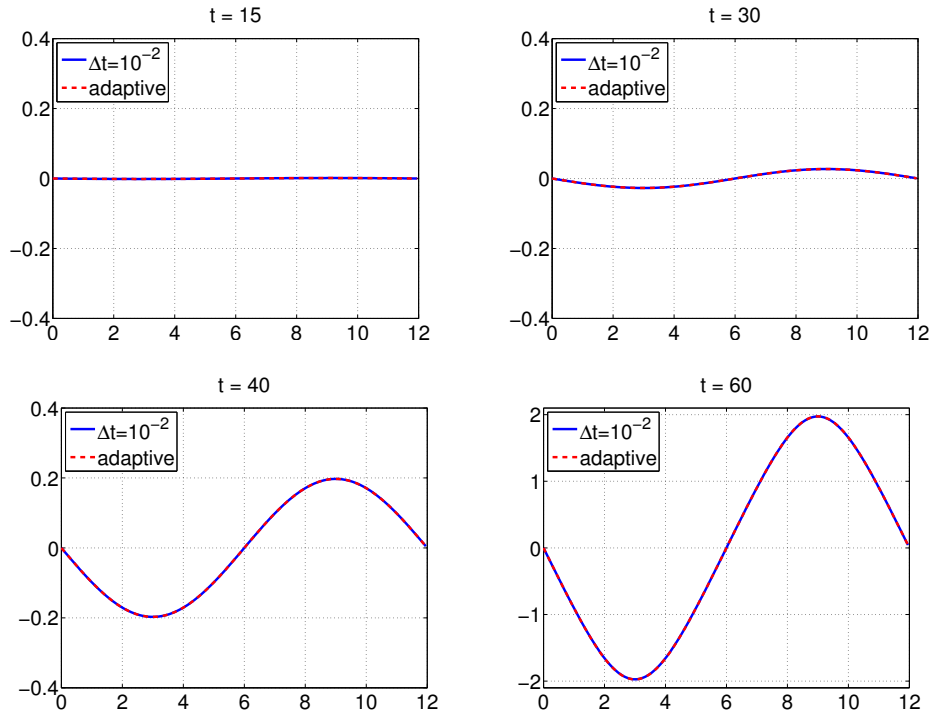

Figure 3.2: Example 1: u computed with $\Delta t = 10^{-2}$ (solid line) and adaptive splitting time-stepping with $\Delta t_{\min} = 10^{-2}$, $\Delta t_{\max} = 10^{-1}$ and $\alpha = 10^3$ (dashed line).

steps are used by the adaptive algorithm. To this end, we plot the splitting steps as a function of time in Figure 3.4. As one can see, the splitting steps are smaller than 10^{-1} only initially and then at the intermediate times. We also compare the CPU times of the adaptive and constant (with $\Delta t = 10^{-2}$) splitting step computations. The results, shown in the first row of Table 3.1, indicate that the CPU time for the adaptive method is about four times smaller than the one for the constant splitting step.

Finally, we test the accuracy of the proposed fast and stable explicit splitting methods. To this end, we perform the mesh-refinement study and measure the L^1- and L^∞-errors. The results reported in Table 3.2 indicate that the experimental convergence rate is close to the expected second-order one. We next fix the splitting step to be very small ($\Delta t = 10^{-3}$) so that the splitting errors do not dominate and perform another mesh-refinement study. The results reported in Table 3.3 show that in this regime, the experimental convergence rate is four, which is the order of

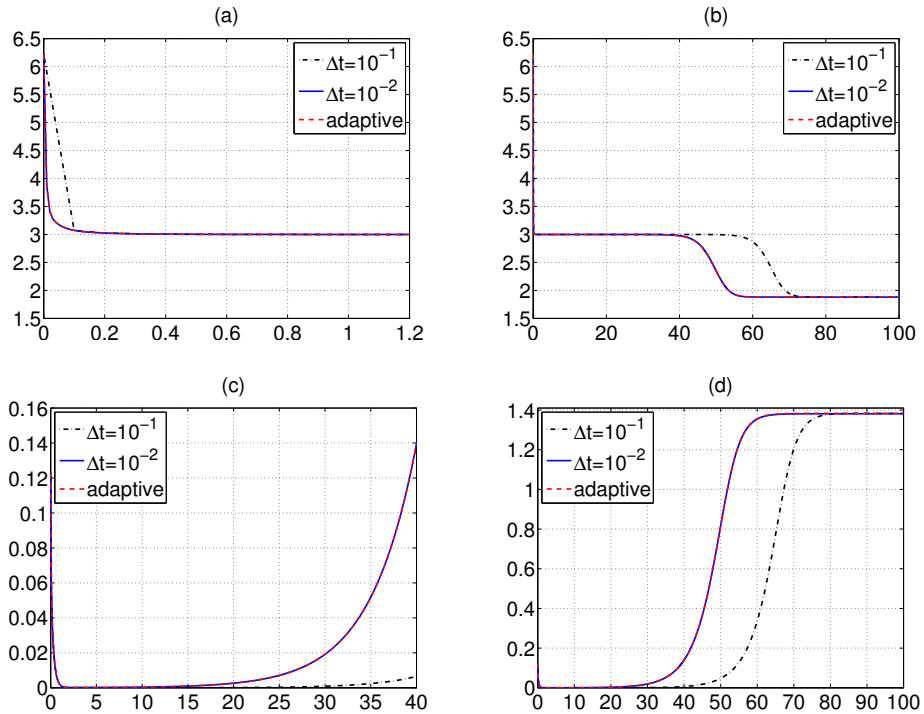

Figure 3.3: Example 1: (a) Energy evolution in a short time period; (b) Energy evolution in a long time period; (c) Roughness development in a time period $t \in [0, 40]$; (d) Roughness development in a long time period. $\Delta t = 10^{-1}$ (dashed dotted line), $\Delta t = 10^{-2}$ (solid line) and adaptive splitting time-stepping with $\Delta t_{\min} = 10^{-2}$, $\Delta t_{\max} = 10^{-1}$ and $\alpha = 10^3$ (dashed line).

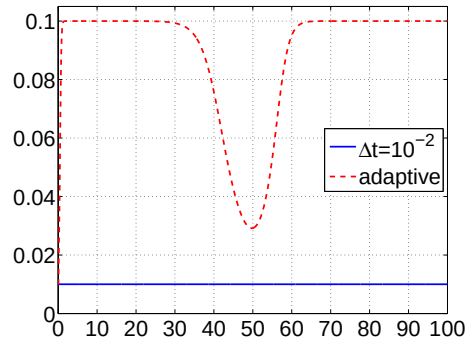

Figure 3.4: Example 1: Splitting step evolution. $\Delta t = 10^{-2}$ (solid line) and adaptive splitting time-stepping with $\Delta t_{\min} = 10^{-2}$, $\Delta t_{\max} = 10^{-1}$ and $\alpha = 10^3$ (dashed line).

finite-difference scheme from Section 3.2.1.

N	Δt	$\|\|u^{N,\Delta t} - u^{N/2,2\Delta t}\|\|_1$	Rate	$\|\|u^{N,\Delta t} - u^{N/2,2\Delta t}\|\|_\infty$	Rate
128	2e-2	3.95e-03	–	7.58e-04	–
256	1e-2	1.07e-03	1.89	2.45e-04	1.63
512	5e-3	2.73e-04	1.97	7.17e-05	1.78
1024	2.5e-3	6.84e-05	1.99	1.93e-05	1.89

Table 3.2: Example 1: L^1- and L^∞-errors and experimental convergence rates at $t = 240$.

N	Δt	$\|\|u^{N,\Delta t} - u^{N/2,\Delta t}\|\|_1$	Rate	$\|\|u^{N,\Delta t} - u^{N/2,\Delta t}\|\|_\infty$	Rate
128	1e-3	8.06e-05	–	2.25e-05	–
256	1e-3	5.18e-06	3.96	1.44e-06	3.96
512	1e-3	3.27e-07	3.99	9.10e-08	3.99
1024	1e-3	2.02e-08	4.02	5.62e-09	4.02

Table 3.3: Example 1: L^1- and L^∞-errors and experimental convergence rates obtained with the fixed small splitting step $\Delta t = 10^{-3}$ at $t = 240$.

Example 2: Two-Dimensional Morphological Instability

Next, we consider the 2-D MBE equation (3.3) with $\delta = 0.1$ subject to the following initial condition:

$$u(x, y, 0) = 0.1(\sin 3x \sin 2y + \sin 5x \sin 5y), \quad (x, y) \in [0, 2\pi] \times [0, 2\pi].$$

This example was studied in [43, 65] to observe the morphological instability due to the nonlinear interaction.

We first compute the solution on a 256×256 uniform grid with the constant splitting step $\Delta t = 10^{-3}$. Figure 3.5 shows the height profiles at times $t = 0, 0.5, 2.5, 5.5, 8$ and 30. The corresponding gradients $|\nabla u|$ are plotted in Figure 3.6. In Figure 3.7, we demonstrate the experimental energy decay and roughness development, which indicate that the solution reaches a steady state at around $t = 12$. The obtained results are in good agreement with those reported in [43].

We then carry out the adaptive strategy to increase the efficiency of the proposed methods. Here, we choose $\Delta t_{\min} = 10^{-3}$, $\Delta t_{\max} = 10^{-2}$ and $\alpha = 10^3$. The

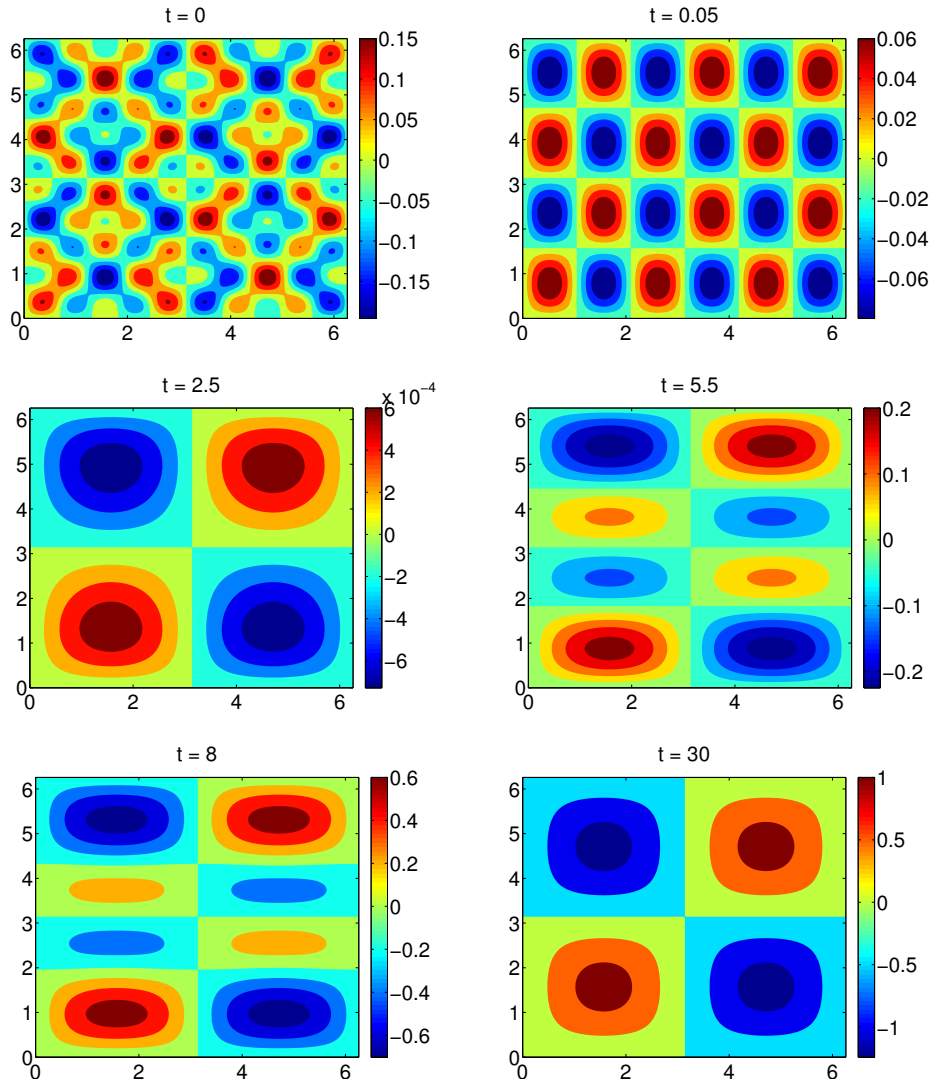

Figure 3.5: Example 2: u computed with $\Delta t = 10^{-3}$.

corresponding energy and roughness curves in Figure 3.7 are practically indistinguishable from those obtained using the small constant splitting step $\Delta t = 10^{-3}$. Splitting steps evolution, plotted in Figure 3.8, shows that $\Delta t \approx \Delta t_{\max}$ when the solution approaches its steady state. This leads to a substantial decrease in CPU time, see the second row in Table 3.1.

Finally, we perform the mesh-refinement study and verify that the experimental convergence rates for the proposed fast and stable explicit operator splitting methods are close to the expected second-order one, see Table 3.4.

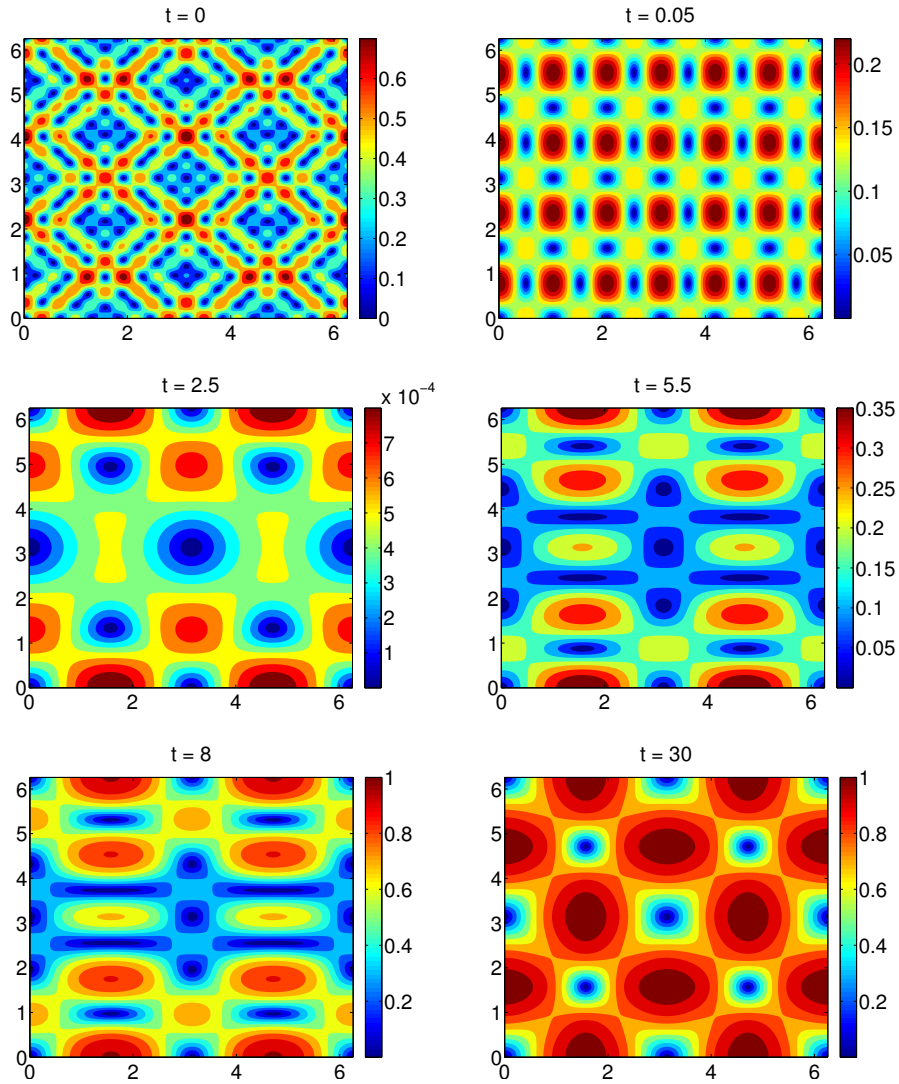

Figure 3.6: Example 2: $|\nabla u|$ computed with $\Delta t = 10^{-3}$.

N	Δt	$\|\|u^{N,\Delta t} - u^{N/2,2\Delta t}\|\|_1$	Rate	$\|\|u^{N,\Delta t} - u^{N/2,2\Delta t}\|\|_\infty$	Rate
64	4e-3	3.36e-03	–	6.01e-04	–
128	2e-3	9.09e-04	1.88	1.55e-04	1.96
256	1e-3	2.48e-04	1.87	4.96e-05	1.64
512	5e-4	6.52e-05	1.93	1.55e-05	1.68

Table 3.4: Example 2: L^1- and L^∞-errors and experimental convergence rates at $t = 30$.

Example 3: Coarsening Dynamics

In this example, we study the 2-D MBE equation (3.3) with $\delta = 1$ subject to initial data, obtained by assigning a uniformly distributed random number in the range

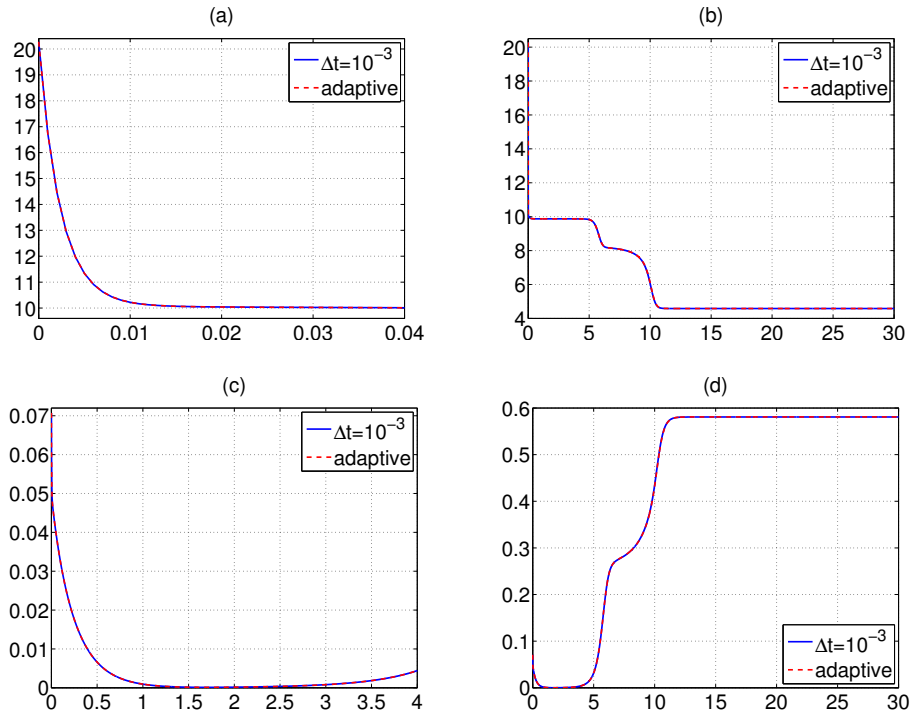

Figure 3.7: Example 2: (a) Energy evolution in a short time period; (b) Energy evolution in a long time period; (c) Roughness development in a short time period; (d) Roughness development in a long time period. $\Delta t = 10^{-3}$ (solid line) and adaptive splitting time-stepping with $\Delta t_{\min} = 10^{-3}$, $\Delta t_{\max} = 10^{-2}$ and $\alpha = 10^3$ (dashed line).

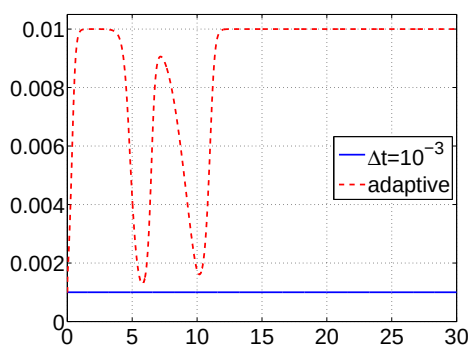

Figure 3.8: Example 2: Splitting step evolution. $\Delta t = 10^{-3}$ (solid line) and adaptive splitting time-stepping with $\Delta t_{\min} = 10^{-3}$, $\Delta t_{\max} = 10^{-2}$ and $\alpha = 10^3$ (dashed line).

$[-0.001, 0.001]$ to each grid point value of $u(x, y, 0)$. We use a 512×512 uniform grid on the computational domain $\Omega = [0, 1000] \times [0, 1000]$.

Figure 3.9 shows the contour lines of the free energy function

$$F_{free} := \frac{1}{4}(|\nabla u| - 1)^2 + \frac{\delta}{2}|\Delta u|^2$$

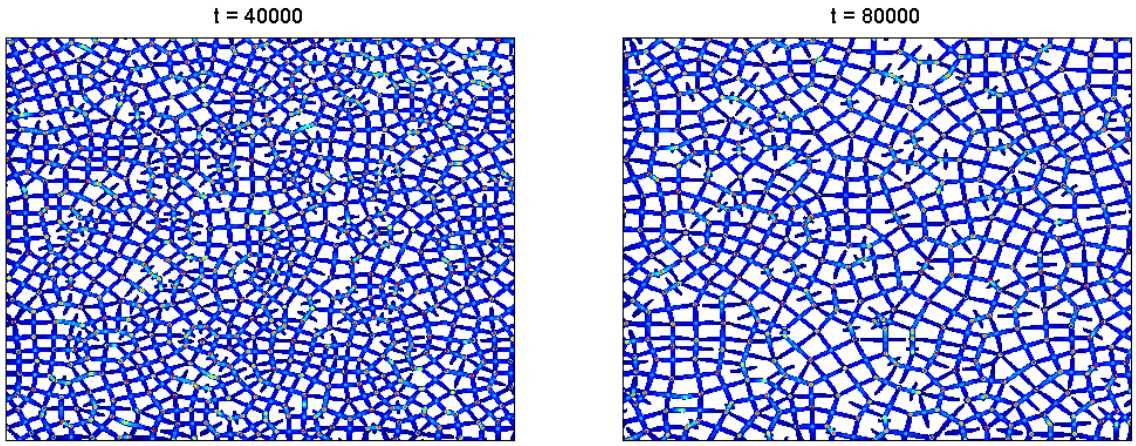

Figure 3.9: Example 3: Contour plots of F_{free} computed with $\Delta t = 10^{-1}$.

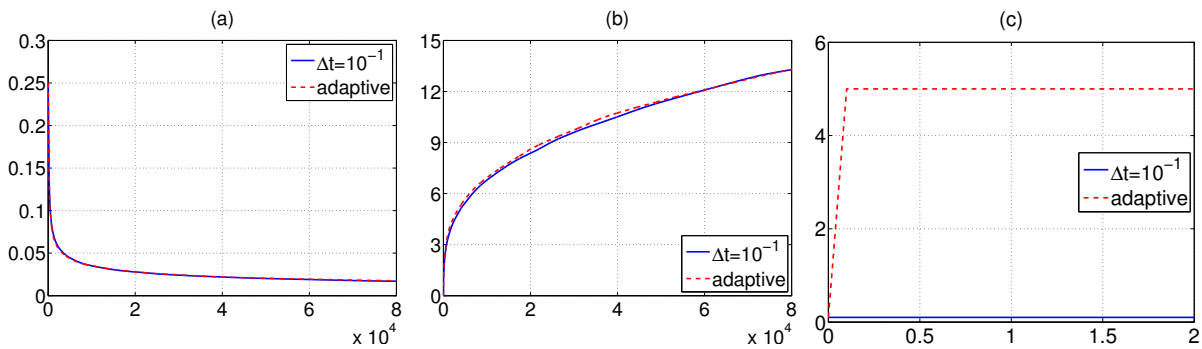

Figure 3.10: Example 3: (a) Energy evolution; (b) Roughness development; (c) Splitting step evolution. $\Delta t = 10^{-1}$ (solid line) and adaptive splitting time-stepping with $\Delta t_{\min} = 10^{-1}$, $\Delta t_{\max} = 5$ and $\alpha = 1$ (dashed line).

at $t = 40,000$ and $80,000$ computed using the constant splitting step $\Delta t = 10^{-1}$. As one can see, the free energy is concentrated on and thus could be used to identify the edges of the pyramidal structures; the pyramid edges form a random network over the surface, which results from the isotropic nature of the surface symmetry; the cells of the network grow in time via a coarsening process.

The energy (3.5), normalized by the domain size, and the roughness (3.35) are plotted in Figure 3.10. To further demonstrate the robustness of the proposed methods, we experimentally verify several important properties of the computed solution. In Figure 3.11 (a), the energy (3.5), normalized by the domain size, is plotted in the log-log scale and it is nearly parallel to the dashed line representing

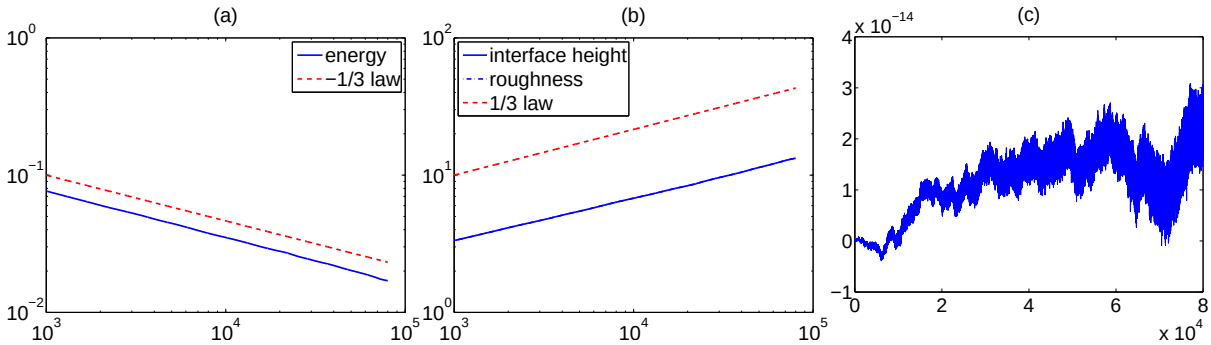

Figure 3.11: Example 3: (a) The log-log scale plot of the energy evolution; (b) The log-log scale plot of the interface height and roughness development; (c) Mean height evolution. In (a)–(c), $\Delta t = 10^{-1}$.

the $t^{-1/3}$ curve. This suggests that the energy decays in time as a power law Ct^n with the exponent $n = -1/3$. In Figure 3.11 (b), the interface height, defined by

$$\widetilde{u}(t) = \left(\frac{1}{|\Omega|} \int_{\Omega} u^2(x, y, t)\, dxdy \right)^{\frac{1}{2}},$$

and the roughness (3.35) are demonstrated to evolve in time according to a power law Ct^n with the exponent $n = 1/3$. Finally, Figure 3.11 (c) suggests that the difference $\bar{u}(t) - \bar{u}(0)$, where the mean height $\bar{u}(t)$ is defined in (3.36), remains practically zero at all times, which implies the mass conservation. The obtained results match the experimental and numerical results reported in [43, 65, 82].

When the adaptive technique with $\Delta t_{\min} = 10^{-1}$, $\Delta t_{\max} = 5$ and $\alpha = 1$ is implemented, the obtained results are very similar. As one can see in Figure 3.10, the splitting step increases to $\Delta t_{\max}$ very soon and then is always selected close to $\Delta t_{\max}$ due to the slow variation of the roughness. This leads to substantial CPU time usage saving, see the third row in Table 3.1.

Remark 3.5.1 We would like to point out that in this example, the curves for the interface height growth and the roughness development in Figure 3.11 (b) almost overlap since $\bar{u}(t) = \bar{u}(0) \approx 0$.

Remark 3.5.2 We would like to stress that in this example, the energy transition

does not occur, and the solution has a smooth variation. It is therefore safe to take a relatively small value $\alpha = 1$ and $\Delta t_{\min} = 10^{-1}$, which is much larger than $\delta/100 = 10^{-2}$.

Example 4—Non-Mean-Zero Initial Data. In this example, taken from [69], we consider the 2-D CH equation (3.4) with $\delta = 0.01$ subject to the following non-mean-zero initial condition:

$$u(x, y, 0) = 0.05 \sin x \sin y + 0.001, \quad (x, y) \in [0, 2\pi] \times [0, 2\pi].$$

We first compute the solution on a 128×128 uniform grid with the constant splitting step $\Delta t = 10^{-3}$. The solution computed at times $t = 1, 2, 5$ and 20 is shown in Figure 3.12 (left). The experimental energy decay and roughness development curves, shown in Figure 3.13, indicate that the solution reaches a steady state at about $t = 9$. These results are in good agreement with those reported in [69].

We then compute the solution using the adaptive strategy with $\Delta t_{\min} = 10^{-3}$, $\Delta t_{\max} = 10^{-2}$ and $\alpha = 10^2$. The results are plotted in Figure 3.12 (right). As one can see, the solution dynamics can be captured correctly when the adaptive strategy is employed. The corresponding energy and roughness curves shown in Figure 3.13 have some discrepancy with those obtained using the small constant splitting step Δt^{-3}, though the adaptive and non-adaptive solutions are quite close and the resulting steady states seem to be the same. Splitting steps evolution, also plotted in Figure 3.13, shows that $\Delta t \approx \Delta t_{\max}$ when the solution approaches its steady state, which leads to a substantial saving in CPU time, see the fourth row in Table 3.1.

Finally, we perform the mesh-refinement study and verify that the experimental convergence rates for the proposed fast and stable explicit operator splitting methods are close to the expected second-order one, see Table 3.5.

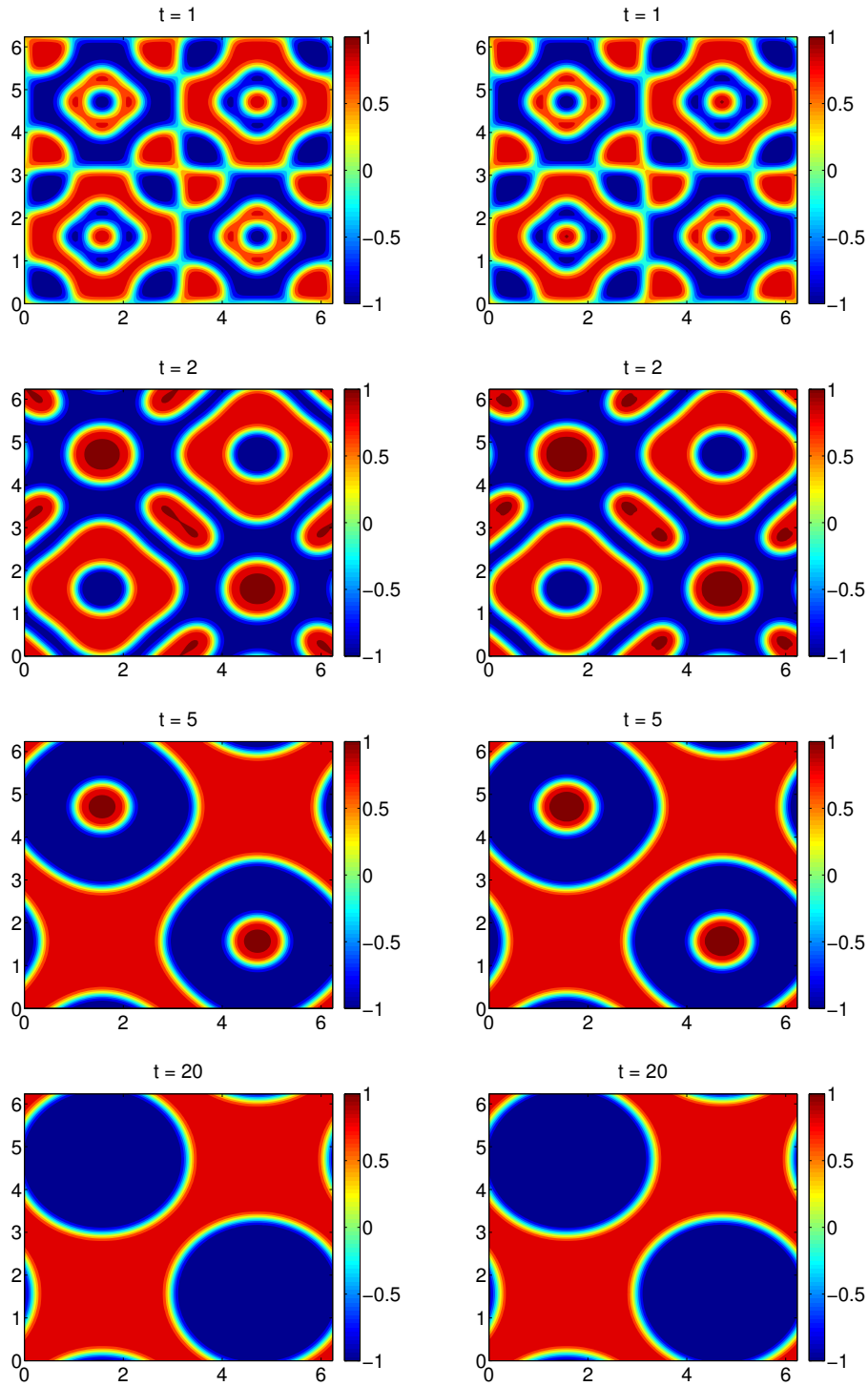

Figure 3.12: Example 4: u computed with $\Delta t = 10^{-3}$ (left column) and adaptive splitting time-stepping with $\Delta t_{\min} = 10^{-3}$, $\Delta t_{\max} = 10^{-2}$ and $\alpha = 10^2$ (right column).

Example 5—Mean-Zero Initial Data. In this example, also taken from [69], we consider the 2-D CH equation with $\delta = 0.01$ subject to the following mean-zero

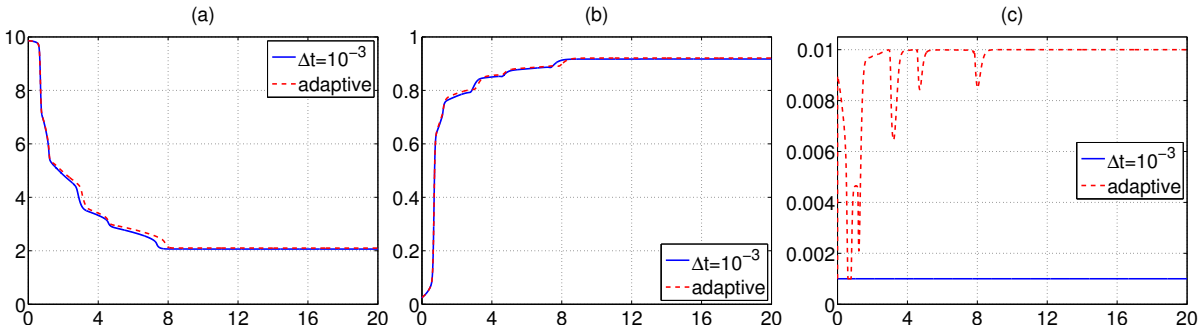

Figure 3.13: Example 4: (a) Energy evolution; (b) Roughness development; (c) Splitting step evolution. $\Delta t = 10^{-3}$ (solid line) and adaptive splitting time-stepping with $\Delta t_{\min} = 10^{-3}$, $\Delta t_{\max} = 10^{-2}$ and $\alpha = 10^2$ (dashed line).

N	Δt	$\|\|u^{N,\Delta t} - u^{N/2,2\Delta t}\|\|_1$	Rate	$\|\|u^{N,\Delta t} - u^{N/2,2\Delta t}\|\|_\infty$	Rate
64	2e-3	1.61e-00	–	3.01e-01	–
128	1e-3	1.37e-01	3.55	2.64e-02	3.51
256	5e-4	3.44e-02	2.00	5.79e-03	2.19
512	2.5e-4	1.12e-02	1.62	1.72e-03	1.75

Table 3.5: Example 4: L^1- and L^∞-errors and experimental convergence rates at $t = 20$.

initial condition:

$$u(x, y, 0) = 0.05 \sin x \sin y, \quad (x, y) \in [0, 2\pi] \times [0, 2\pi].$$

We first use a uniform 128×128 grid with a constant splitting step $\Delta t = 10^{-3}$ and compute the solution until a large final time $t = 100$. The obtained results are shown in Figure 3.14 (left column). Even though the solution at a small time $t = 2$ is similar to the corresponding solution reported in [68], later on our solution bifurcates and seems to converge to a different steady state. We therefore perform a thorough comparative study by taking a smaller $\Delta t = 10^{-4}$ and finer 256×256 grid. The results, plotted in Figure 3.14, clearly indicate that different numerical solutions may converge to different steady states. We then use the sixth-order semi-discrete finite-difference scheme for equation (3.11) instead of the fourth-order one and discover even more different steady-state patterns, see Figure 3.15.

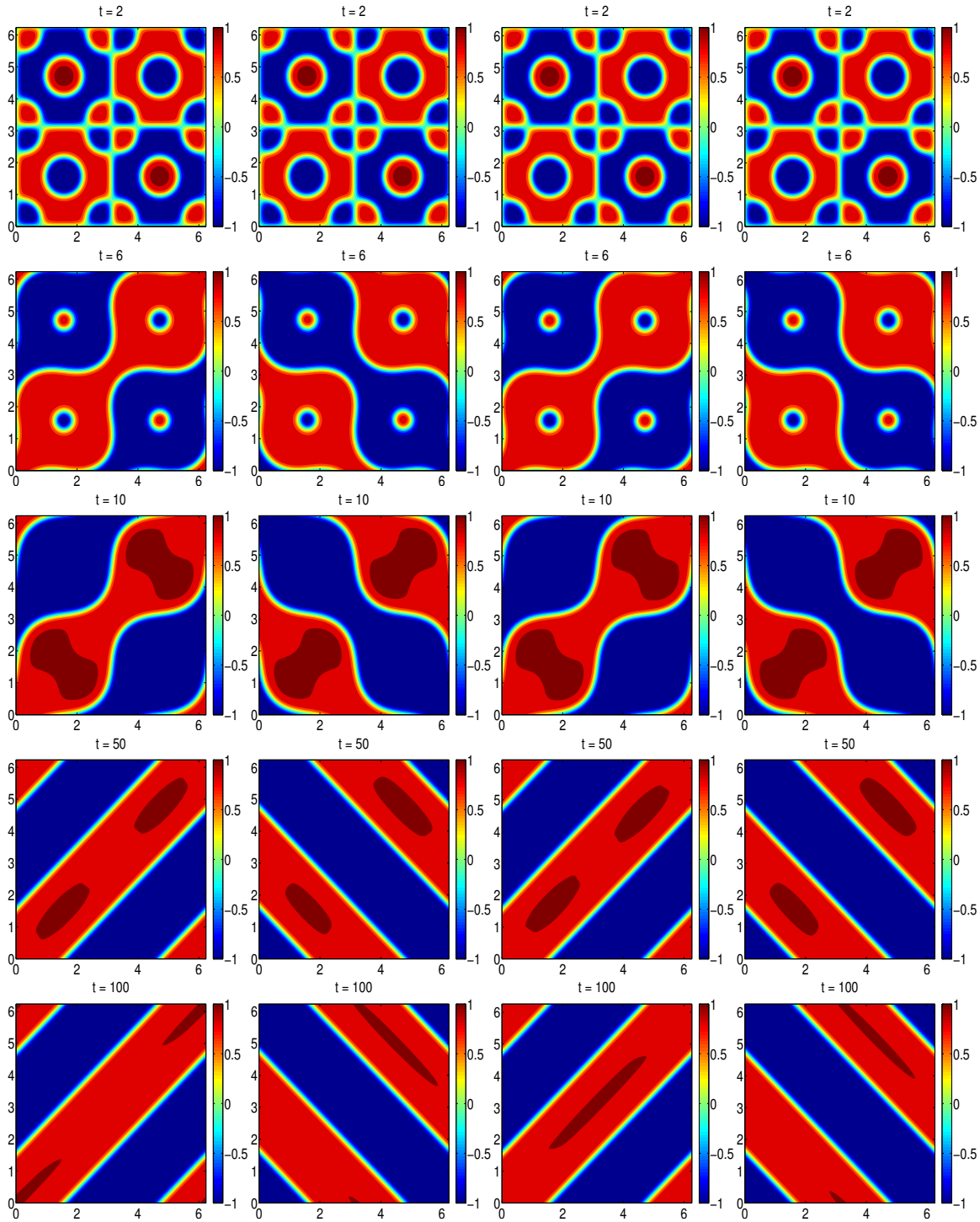

Figure 3.14: Example 5: u computed with a 128×128 grid, $\Delta t = 10^{-3}$ (first column); 128×128 grid, $\Delta t = 10^{-4}$ (second column); 256×256 grid, $\Delta t = 10^{-3}$ (third column); 256×256 grid, $\Delta t = 10^{-4}$ (fourth column).

Our results suggest that the mean-zero solutions of the 2-D CH equation (3.4) may be unstable. Our conjecture is supported by recent analytical results on

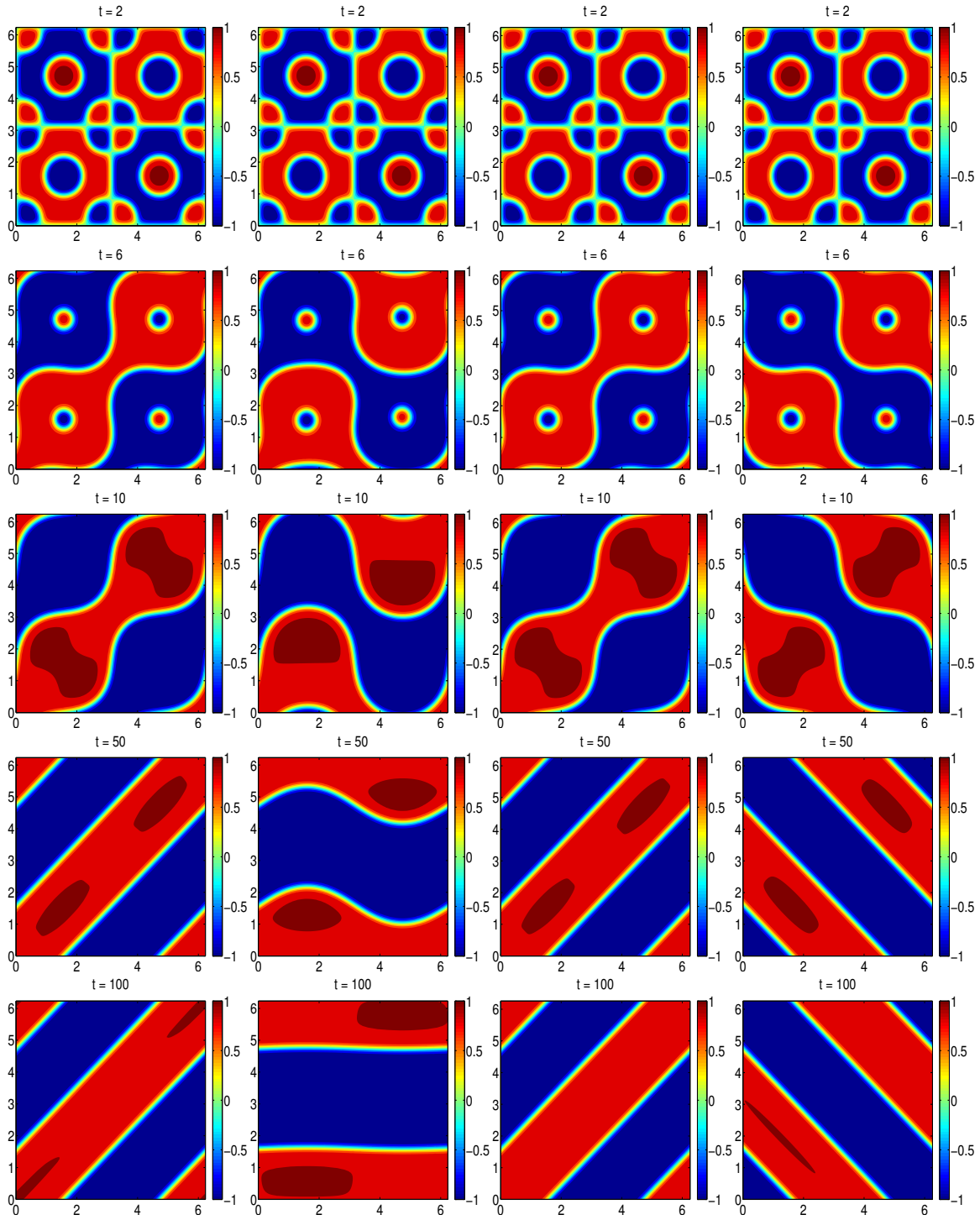

Figure 3.15: Example 5: Same as in Figure 3.14, but using the sixth-order scheme for (3.11).

unstable equilibria in the 1-D CH equation, see [83].

Appendix A

Proofs of Theorems 3.2.4–3.2.6

Here, we provide proofs of Theorem 3.2.4–3.2.6. We denote $t^{\text{new}} := t + \Delta t_{\text{FE}}$. We also use the following notations: $u_j^{\text{new}} := u(x_j, t + \Delta t_{\text{FE}})$ (in Theorem 3.2.4) and $u_{j,k}^{\text{new}} := u(x_j, y_k, t + \Delta t_{\text{FE}})$ (in Theorems 3.2.5 and 3.2.6).

A.1 Proof of Theorem 3.2.4 (1-D MBE Equation)

Applying the forward Euler method to discretize (3.16) results in

$$\frac{u_j^{\text{new}} - u_j}{\Delta t} = F_j. \tag{A.1}$$

We first multiply both sides of equation (A.1) by $(u_j^{\text{new}} + u_j)/2$, replace u_j^{new} on the right using (A.1) and sum over the entire domain to obtain

$$\sum_j \frac{(u_j^{\text{new}})^2 - u_j^2}{2\Delta t} = \sum_j F_j u_j + \frac{\Delta t}{2} \sum_j F_j^2. \tag{A.2}$$

We then rewrite the first term on the right-hand side (RHS) of (A.2) as follows:

$$\begin{aligned}\sum_j F_j u_j &\overset{(3.16)}{=} \sum_j \sum_{p=-m}^{m} \alpha_p H_{j+p} u_j = \sum_{p=-m}^{m} \alpha_p \sum_j H_{j+p} u_j = \sum_{p=-m}^{m} \alpha_p \sum_j H_j u_{j-p} \\ &= \sum_j H_j \sum_{p=-m}^{m} \alpha_p u_{j-p} = \sum_j H_j \sum_{p=-m}^{m} \alpha_{-p} u_{j+p} \\ &\overset{(3.18)}{=} \sum_j H_j \sum_{p=-m}^{m} (-\alpha_p) u_{j+p} \overset{(3.17)}{=} -\sum_j (u_x)_j^4,\end{aligned}$$

and estimate the second term on the RHS of (A.2) using the Cauchy-Schwarz inequality:

$$\begin{aligned}\sum_j F_j^2 &\overset{(3.16)}{=} \sum_j \left(\sum_{p=-m}^{m} \alpha_p H_{j+p} \right)^2 \leq 2m \sum_j \sum_{p=-m}^{m} \alpha_p^2 H_{j+p}^2 \\ &= 2m \sum_{p=-m}^{m} \alpha_p^2 \sum_j H_{j+p}^2 = 2am \sum_j H_j^2 \overset{(3.17)}{=} 2am \sum_j (u_x)_j^6.\end{aligned}$$

Therefore, the left-hand side (LHS) of equation (A.2) can be bounded by

$$\sum_j \frac{(u_j^{\text{new}})^2 - u_j^2}{2\Delta t} \leq -\sum_j (u_x)_j^4 + am\Delta t \sum_j (u_x)_j^6 \leq \left[am\Delta t \max_j (u_x)_j^2 - 1 \right] \sum_j (u_x)_j^4,$$

which is nonpositive provided the time-step is bounded by (3.26). ■

A.2 Proof of Theorem 3.2.5 (2-D MBE Equation)

Applying the forward Euler method to discretize (3.20) results in

$$\frac{u_{j,k}^{\text{new}} - u_{j,k}}{\Delta t} = F_{j,k}. \tag{A.3}$$

We first multiply both sides of equation (A.3) by $(u_{j,k}^{\text{new}} + u_{j,k})/2$, replace $u_{j,k}^{\text{new}}$ on the right using (A.3) and sum over the entire domain to obtain

$$\sum_{j,k} \frac{(u_{j,k}^{\text{new}})^2 - u_{j,k}^2}{2\Delta t} = \sum_{j,k} F_{j,k} u_{j,k} + \frac{\Delta t}{2} \sum_{j,k} F_{j,k}^2. \tag{A.4}$$

We then use (3.20)–(3.22) to rewrite the first term on the RHS of (A.4) as follows:

$$\sum_{j,k} F_{j,k} u_{j,k} = -\sum_{j,k} \left[(u_x)_{j,k}^4 + (u_x)_{j,k}^2 (u_y)_{j,k}^2 \right] - \sum_{j,k} \left[(u_y)_{j,k}^4 + (u_y)_{j,k}^2 (u_x)_{j,k}^2 \right],$$

and use (3.20), (3.21) and the Cauchy-Schwarz inequality to estimate the second term on the RHS of (A.4):

$$\sum_{j,k} F_{j,k}^2 \leq 8am \sum_{j,k} \left[(u_x)_{j,k}^6 + (u_x)_{j,k}^2 (u_y)_{j,k}^4 \right] + 8bm \sum_{j,k} \left[(u_y)_{j,k}^6 + (u_y)_{j,k}^2 (u_x)_{j,k}^4 \right].$$

Therefore, the LHS of equation (A.4) can be bounded by

$$\begin{aligned}
&\sum_{j,k} \frac{(u_{j,k}^{\text{new}})^2 - u_{j,k}^2}{2\Delta t} \\
&\quad \leq \left[4am\Delta t \max_{j,k} (u_x)_{j,k}^2 - 1 \right] \sum_{j,k} (u_x)_{j,k}^4 + \left[4bm\Delta t \max_{j,k} (u_y)_{j,k}^2 - 1 \right] \sum_{j,k} (u_y)_{j,k}^4 \\
&\quad + \left[4am\Delta t \max_{j,k} (u_y)_{j,k}^2 - 1 \right] \sum_{j,k} (u_x)_{j,k}^2 (u_y)_{j,k}^2 \\
&\quad + \left[4bm\Delta t \max_{j,k} (u_x)_{j,k}^2 - 1 \right] \sum_{j,k} (u_y)_{j,k}^2 (u_x)_{j,k}^2,
\end{aligned}$$

which is nonpositive provided the time-step is bounded by (3.28). ■

A.3 Proof of Theorem 3.2.6 (2-D CH Equation)

Applying the forward Euler method to discretize (3.24) results in

$$\frac{u_{j,k}^{\text{new}} - u_{j,k}}{\Delta t} = F_{j,k}. \tag{A.5}$$

Once again, we multiply both sides of equation (A.5) by $(u_{j,k}^{\text{new}} + u_{j,k})/2$, replace $u_{j,k}^{\text{new}}$ on the right using (A.5) and sum over the entire domain to obtain

$$\sum_{j,k} \frac{(u_{j,k}^{\text{new}})^2 - u_{j,k}^2}{2\Delta t} = \sum_{j,k} F_{j,k} u_{j,k} + \frac{\Delta t}{2} \sum_{j,k} F_{j,k}^2. \tag{A.6}$$

We now notice that within the accuracy of the scheme

$$H_{j,k}^x = 3u_{j,k}^2 (u_x)_{j,k} \quad \text{and} \quad H_{j,k}^y = 3u_{j,k}^2 (u_y)_{j,k}. \tag{A.7}$$

We then use (A.7), (3.23) and (3.24) to rewrite the first term on the RHS of (A.6) as follows:

$$\sum_{j,k} F_{j,k} u_{j,k} = -3 \sum_{j,k} u_{j,k}^2 (u_x)_{j,k}^2 - 3 \sum_{j,k} u_{j,k}^2 (u_y)_{j,k}^2,$$

and use (A.7), (3.24) and the Cauchy-Schwarz inequality to estimate the second term on the RHS of (A.6):

$$\sum_{j,k} F_{j,k}^2 \leq 36am \sum_{j,k} u_{j,k}^4 (u_x)_{j,k}^2 + 36bm \sum_{j,k} u_{j,k}^4 (u_y)_{j,k}^2.$$

Therefore, the LHS of equation (A.6) can be bounded by

$$\begin{aligned} \sum_{j,k} \frac{(u_{j,k}^{\text{new}})^2 - u_{j,k}^2}{2\Delta t} \leq\ & 3 \left[6am\Delta t \max_{j,k}(u_{j,k}^2) - 1 \right] \sum_{j,k} u_{j,k}^2 (u_x)_{j,k}^2 \\ & + 3 \left[6bm\Delta t \max_{j,k}(u_{j,k}^2) - 1 \right] \sum_{j,k} u_{j,k}^2 (u_y)_{j,k}^2, \end{aligned}$$

which is nonnegative provided the time-step is bounded by (3.30). ■

Bibliography

[1] C.-Y. Kao, A. Kurganov, Z. Qu, and Y. Wang. A fast explicit operator splitting method for modified buckley–leverett equations. *Journal of Scientific Computing*, 64(3):837–857, 2015.

[2] Y. Cheng, A. Kurganov, Z. Qu, and T. Tang. Fast and stable explicit operator splitting methods for phase-field models. *Journal of Computational Physics*, 303:45–65, 2015.

[3] A. Chertock, A. Kurganov, Z. Qu, and T. Wu. Three-layer approximation of two-layer shallow water equations. *Mathematical Modelling and Analysis*, 18(5):675–693, 2013.

[4] H. F. Trotter. On the product of semi-groups of operators. *Proceedings of the American Mathematical Society*, 10(4):545–551, 1959.

[5] G. I. Marchuk. *Metody rasshchepleniya.* (Russian) [Splitting Methods] "Nauka", Moscow, 1988.

[6] G. I. Marchuk. Splitting and alternating direction methods. In *Handbook of numerical analysis, Vol. I*, Handb. Numer. Anal., I, pages 197–462. North-Holland, Amsterdam, 1990.

[7] G. Strang. On the construction and comparison of difference schemes. *SIAM J. Numer. Anal.*, 5:506–517, 1968.

[8] D. Goldman and T. J. Kaper. N th-order operator splitting schemes and nonreversible systems. *SIAM journal on numerical analysis*, 33(1):349–367, 1996.

[9] Q. Sheng. Solving linear partial differential equations by exponential splitting. *IMA Journal of numerical analysis*, 9(2):199–212, 1989.

[10] H. Jia and K. Li. A third accurate operator splitting method. *Mathematical and Computer Modelling*, 53(1):387–396, 2011.

[11] S. Descombes. Convergence of a splitting method of high order for reaction-diffusion systems. *Mathematics of Computation*, 70(236):1481–1501, 2001.

[12] A. D. Bandrauk, E. Dehghanian, and H. Lu. Complex integration steps in decomposition of quantum exponential evolution operators. *Chemical physics letters*, 419(4):346–350, 2006.

[13] J. Chambers. Symplectic integrators with complex time steps. *The Astronomical Journal*, 126(2):1119, 2003.

[14] Z. Gegechkori, J. Rogava, and M. Tsiklauri. High degree precision decomposition method for the evolution problem with an operator under a split form. *ESAIM: Mathematical Modelling and Numerical Analysis-Modélisation Mathématique et Analyse Numérique*, 36(4):693–704, 2002.

[15] Z. Gegechkori, J. Rogava, and M. Tsiklauri. The fourth order accuracy decomposition scheme for an evolution problem. *ESAIM: Mathematical Modelling and Numerical Analysis*, 38(04):707–722, 2004.

[16] M. Suzuki. General theory of fractal path integrals with applications to many-body theories and statistical physics. *Journal of Mathematical Physics*, 32(2):400–407, 1991.

[17] F. Castella, P. Chartier, S. Descombes, and G. Vilmart. Splitting methods with complex times for parabolic equations. *BIT Numerical Mathematics*, 49(3):487–508, 2009.

[18] A. Chertock, C. Doering, E. Kashdan, and A. Kurganov. A fast explicit operator splitting method for passive scalar advection. *J. Sci. Comput.*, 45:200–214, 2010.

[19] A. Chertock, E. Kashdan, and A. Kurganov. Propagation of diffusing pollutant by a hybrid Eulerian-Lagrangian method. In *Hyperbolic problems: theory, numerics, applications*, pages 371–379. Springer, Berlin, 2008.

[20] A. Chertock, A. Kurganov, and G. Petrova. Fast explicit operator splitting method. Application to the polymer system. In *Finite volumes for complex applications IV*, pages 63–72. ISTE, London, 2005.

[21] A. Chertock, A. Kurganov, and G. Petrova. Fast explicit operator splitting method for convection-diffusion equations. *Internat. J. Numer. Meth. Fluids*, 59:309–332, 2009.

[22] A. Chertock and A. Kurganov. On splitting-based numerical methods for convection-diffusion equations. In *Numerical methods for balance laws*, volume 24 of *Quad. Mat.*, pages 303–343. Dept. Math., Seconda Univ. Napoli, Caserta, 2009.

[23] E. F. Toro. *Riemann solvers and numerical methods for fluid dynamics: a practical introduction.* Springer Science & Business Media, 2013.

[24] R. LeVeque. *Finite volume methods for hyperbolic problems*. Cambridge Texts in Applied Mathematics. Cambridge University Press, Cambridge, 2002.

[25] Numerical schemes for conservation laws, author=Kröner, D, journal=Wiley-Teubner Series Advances in Numerical Mathematics, year=1997, publisher=John Wiley & Sons Ltd., Chichester.

[26] E. Godlewski and P.-A. Raviart. *Numerical approximation of hyperbolic systems of conservation laws*, volume 118. Springer Science & Business Media, 2013.

[27] F. Bouchut. *Nonlinear stability of finite Volume Methods for hyperbolic conservation laws: And Well-Balanced schemes for sources*. Springer Science & Business Media, 2004.

[28] M. Ben-Artzi and J. Falcovitz. *Generalized Riemann problems in computational fluid dynamics*, volume 11. Cambridge University Press, 2003.

[29] A. Kurganov and C.-T. Lin. On the reduction of numerical dissipation in central-upwind schemes. *Commun. Comput. Phys.*, 2(1):141–163, 2007.

[30] A. Kurganov, S. Noelle, and G. Petrova. Semidiscrete central-upwind schemes for hyperbolic conservation laws and Hamilton-Jacobi equations. *SIAM J. Sci. Comput.*, 23(3):707–740 (electronic), 2001.

[31] A. Kurganov and E. Tadmor. New high resolution central schemes for nonlinear conservation laws and convection-diffusion equations. *J. Comput. Phys.*, 160:241–282, 2000.

[32] U. M. Ascher and L. R. Petzold. *Computer methods for ordinary differential equations and differential-algebraic equations*. Society for Industrial and Applied Mathematics (SIAM), Philadelphia, PA, 1998.

[33] E. Hairer and G. Wanner. *Solving ordinary differential equations. II*, volume 14 of *Springer Series in Computational Mathematics*. Springer-Verlag, Berlin, second edition, 1996. Stiff and differential-algebraic problems.

[34] A. Abdulle and A. A. Medovikov. Second order chebyshev methods based on orthogonal polynomials. *Numerische Mathematik*, 90(1):1–18, 2001.

[35] A. Abdulle. Fourth order Chebyshev methods with recurrence relation. *SIAM J. Sci. Comput.*, 23(6):2041–2054 (electronic), 2002.

[36] W. Hundsdorfer and J. G. Verwer. *Numerical solution of time-dependent advection-diffusion-reaction equations*, volume 33. 2013.

[37] A. Medovikov. High order explicit methods for parabolic equations. *BIT*, 38(2):372–390, 1998.

[38] U. M. Ascher, S. J. Ruuth, and R. J. Spiteri. Implicit-explicit runge-kutta methods for time-dependent partial differential equations. *Applied Numerical Mathematics*, 25(2):151–167, 1997.

[39] C. J. van Duijn, L. A. Peletier, and I. S. Pop. A new class of entropy solutions of the Buckley-Leverett equation. *SIAM J. Math. Anal.*, 39(2):507–536 (electronic), 2007.

[40] Y. Wang. *Central schemes for the modified Buckley-Leverett equation.* PhD thesis, The Ohio State University, 2010.

[41] Y. Wang and C.-Y. Kao. Central schemes for the modified Buckley-Leverett equation. *J. Comput. Sci.*, 4(1):12–23, 2013.

[42] J. W. Cahn and J. E. Hilliard. Free energy of a nonuniform system. I. interfacial free energy. *J. Chem. Phys.*, 28:258–267, 1958.

[43] B. Li and J.-G. Liu. Thin film epitaxy with or without slope selection. *Euro. Jnl of Applied Mathematics*, 14:713–743, 2003.

[44] S. E. Buckley and M. C. Leverett. Mechanism of fluid displacement in sands. *Petroleum Transactions, AIME*, 146:107–116, 1942.

[45] D. A. DiCarlo. Experimental measurements of saturation overshoot on infiltration. *Water Resour. Res.*, 40(4):W04215.1–W04215.9, 2004.

[46] S. M. Hassanizadeh and W. G. Gray. Mechanics and thermodynamics of multiphase flow in porous media including interphase boundaries. *Adv. Water Resour.*, 13:169–186, 1990.

[47] S. Hassanizadeh and W. G. Gray. Thermodynamic basis of capillary pressure in porous media. *Water Resour. Res.*, 29:3389–3405, 1993.

[48] G. I. Barenblatt, J. Garcia-Azorero, A. De Pablo, and J. L. Vazquez. Mathematical model of the non-equilibrium water-oil displacement in porous strata. *Appl. Anal.*, 65(1-2):19–45, 1997.

[49] K. Spayd and M. Shearer. The Buckley-Leverett equation with dynamic capillary pressure. *SIAM J. Appl. Math.*, 71(4):1088–1108, 2011.

[50] A. Kurganov, G. Petrova, and B. Popov. Adaptive semi-discrete central-upwind schemes for nonconvex hyperbolic conservation laws. *SIAM J. Sci. Comput.*, 29:2381–2401, 2007.

[51] A. Chertock, A. Kurganov, and G. Petrova. Fast explicit operator splitting method for convection-diffusion equations. *Internat. J. Numer. Meth. Fluids*, 59:309–332, 2009.

[52] C. J. van Duijn, A. Mikelić, and I. S. Pop. Effective equations for two-phase flow with trapping on the micro scale. *SIAM J. Appl. Math.*, 62(5):1531–1568 (electronic), 2002.

[53] C. J. van Duijn, A. Mikelic, and I. S. Pop. Effective Buckley-Leverett equations by homogenization. In *Progress in industrial mathematics at ECMI 2000 (Palermo)*, volume 1 of *Math. Ind.*, pages 42–51. Springer, Berlin, 2002.

[54] A. J. Wathen. *Moving finite elements and oil reseruoir modelàng*. PhD thesis, University of Reading, U.K., 1984.

[55] I. W. Johnson, A. J. Wathen, and M. J. Baines. Moving finite element methods for evolutionary problems. II. Applications. *J. Comput. Phys.*, 79(2):270–297, 1988.

[56] C. Cuesta, C. J. van Duijn, and J. Hulshof. Infiltration in porous media with dynamic capillary pressure: travelling waves. *European J. Appl. Math.*, 11(4):381–397, 2000.

[57] K.-A. Lie and S. Noelle. On the artificial compression method for second-order nonoscillatory central difference schemes for systems of conservation laws. *SIAM J. Sci. Comput.*, 24(4):1157–1174, 2003.

[58] H. Nessyahu and E. Tadmor. Nonoscillatory central differencing for hyperbolic conservation laws. *J. Comput. Phys.*, 87(2):408–463, 1990.

[59] P. K. Sweby. High resolution schemes using flux limiters for hyperbolic conservation laws. *SIAM J. Numer. Anal.*, 21(5):995–1011, 1984.

[60] B. van Leer. Towards the ultimate conservative difference scheme. V. A second-order sequel to Godunov's method. *J. Comput. Phys.*, 32(1):101–136, 1979.

[61] C.-W. Shu. Essentially non-oscillatory and weighted essentially non-oscillatory schemes for hyperbolic conservation laws. In *Advanced numerical approximation of nonlinear hyperbolic equations (Cetraro, 1997)*, volume 1697 of *Lecture Notes in Math.*, pages 325–432. Springer, Berlin, 1998.

[62] C.-W. Shu. High order weighted essentially nonoscillatory schemes for convection dominated problems. *SIAM Rev.*, 51(1):82–126, 2009.

[63] S. Gottlieb, D. Ketcheson, and C.-W. Shu. *Strong stability preserving Runge-Kutta and multistep time discretizations*. World Scientific Publishing Co. Pte. Ltd., Hackensack, NJ, 2011.

[64] S. Gottlieb, C.-W. Shu, and E. Tadmor. Strong stability-preserving high-order time discretization methods. *SIAM Rev.*, 43(1):89–112, 2001.

[65] C. Xu and T. Tang. Stability analysis of large time-stepping methods for epitaxial growth models. *SIAM J. Numer. Anal.*, 44:1759–1779, 2006.

[66] Y. He, Y. Liu, and T. Tang. On large time-stepping methods for the Cahn-Hilliard equation. *Appl. Numer. Math.*, 57:616–628, 2007.

[67] Z. Qiao, Z. Zhang, and T. Tang. An adaptive time-stepping strategy for the molecular beam epitaxy models. *SIAM J. Sci. Comput.*, 33:1395–1414, 2011.

[68] Z. Zhang and Z. Qiao. An adaptive time-stepping strategy for the Cahn-Hilliard equation. *Commun. Comput. Phys.*, 1:1261–1278, 2012.

[69] X. Feng, T. Tang, and J. Yang. Long time numerical simulations for phase-field problems using p-adaptive spectral deferred correction methods. *SIAM J. Sci. Comput.*, 37(1):A271–A294, 2015.

[70] J. Shen, C. Wang, X. Wang, and S. M. Wise. Second-order convex splitting schemes for gradient flows with Ehrlich-Schwoebel type energy: application to thin film epitaxy. *SIAM J. Numer. Anal.*, 50(1):105–125, 2012.

[71] F. Guillén-González and G. Tierra. Second order schemes and time-step adaptivity for Allen-Cahn and Cahn-Hilliard models. *Comput. Math. Appl.*, 68(8):821–846, 2014.

[72] F. Guillén-González and G. Tierra. On linear schemes for a Cahn-Hilliard diffuse interface model. *J. Comput. Phys.*, 234:140–171, 2013.

[73] G. Tierra and F. Guillén-González. Numerical methods for solving the Cahn-Hilliard equation and its applicability to related energy-based models. *Arch. Comput. Methods Eng.*, 22(2):269–289, 2015.

[74] A. Abdulle and A. A. Medovikov. Second order Chebyshev methods based on orthogonal polynomials. *Numer. Math.*, 90(1):1–18, 2001.

[75] W. Hundsdorfer and J. Verwer. *Numerical solution of time-dependent advection-diffusion-reaction equations*, volume 33 of *Springer Series in Computational Mathematics*. Springer-Verlag, Berlin, 2003.

[76] A. Abdulle. ROCK4 code available at `http://www.unige.ch/ hairer/software.html`.

[77] A. A. Medovikov. DUMKA3 code available at `http://dumkaland.org/`.

[78] B. P. Sommeijer, L. F. Shampine, and J. G. Verwer. RKC: an explicit solver for parabolic PDEs. *J. Comput. Appl. Math.*, 88(2):315–326, 1998.

[79] P. J. van der Houwen and B. P. Sommeijer. On the internal stability of explicit, m-stage Runge-Kutta methods for large m-values. *Z. Angew. Math. Mech.*, 60(10):479–485, 1980.

[80] J. G. Verwer, W. H. Hundsdorfer, and B. P. Sommeijer. Convergence properties of the Runge-Kutta-Chebyshev method. *Numer. Math.*, 57(2):157–178, 1990.

[81] J. G. Verwer, B. P. Sommeijer, and W. Hundsdorfer. RKC time-stepping for advection-diffusion-reaction problems. *J. Comput. Phys.*, 201(1):61–79, 2004.

[82] D. Moldovan and L. Golubovic. Interfacial coarsening dynamics in epitaxial growth with slope selection. *Phys. Rev. E*, 61(6):6190C6214, 2000.

[83] A. Scheel. Spinodal decomposition and coarsening fronts in the cahn–hilliard equation. *Journal of Dynamics and Differential Equations*, pages 1–34, 2014.

Biography

Zhuolin Qu was born in Shanghai, China in 1989. She attended the School of Mathematical Science in University of Science and Technology of China, where she graduated with Bachelor of Science degree in Mathematics in 2011. She then enrolled in PhD program under the guidance of Dr. Alexander Kurganov at Mathematics Department in Tulane University.